Chapter 7
Fundamentals of 3D Images

Until now, we have covered the fundamentals of X-rays and then, sequentially learned about image reconstruction, various component devices, various applied technologies, and the realities of 3D imaging. Now, we finally envision the actual process of conducting 3D imaging. Applying what we have learned until now, we select a suitable device in the case of an industrial X-ray CT and set up suitable component devices in the case of synchrotron radiation X-ray tomography. Imaging conditions should be firmly established based on solid foundational knowledge and guidelines. If the device used is one of the latest industrial X-ray CT scanners, then user-friendly software may automatically determine imaging conditions to some extent. However, the ability to independently determine imaging success by looking at the obtained 3D image and pursuing more favorable conditions can make a significant difference in whether the imaging in X-ray tomography was successful.

X-ray tomography has been the traditional choice for imaging complex internal or external structures, items with parts having varying degrees of X-ray absorption, or items with complex regions or microstructures. It is difficult in such cases to obtain images with optimal image quality using imaging conditions that are consistently the same, pre-determined, or completely automatic. Furthermore, X-ray tomography generates unique artifacts in the obtained 3D image. Understanding this is also an essential component. Furthermore, it is often the case with industrial X-ray CT scanners or synchrotron radiation X-ray tomography that various material or sample sizes must be handled with a single device. In contrast, the subjects of medical X-ray CT scanners are restricted to human bodies and all hospitals seek to diagnose illnesses in the same organ with the same image quality standard. For this reason, image quality assessments that are unique to the device are important for medical X-ray CT scanners. However, the image quality assessments of each 3D image obtained when various material and sample sizes are used are essential with industrial X-ray CT scanners or synchrotron radiation X-ray tomography. It is through suitable image quality assessments that researchers and engineers can determine whether the 3D image sufficiently reflects the internal structure to be observed or where the observable limits apply to the size and contrast.

H. Toda, *X-Ray CT*,
https://doi.org/10.1007/978-981-16-0590-1_7

The objective of this chapter is to develop a deeper understanding of 3D imaging, conducting a simple examination of the images obtained to gain a general understanding of the advantages and disadvantages of the approach and of the defects that can occur during the process. We will also devote space in this chapter to a more detailed analysis of 3D imaging, as well as a quantitative understanding of its pros and cons.

7.1 3D Image Structure

The 3D picture element that corresponds to the *pixel* that comprises a 2D image is referred to as a *voxel*. A voxel is not necessarily a cube. Until the miniaturization of line sensor camera elements, it was typical for medical X-ray CT scanners to have *anisotropic voxels* (Fig. 7.1b for reference) whose measurement pitch in the human body axis direction (i.e. slice thickness) was long. Industrial X-ray CT scanners and synchrotron radiation X-ray tomography typically generate 3D images comprising cubic *isotropic voxels* (Fig. 7.1a for reference) using 2D detectors. In this case, the voxel size of the 3D image is stipulated by the effective pixel size (so-called pixel size) determined by the vertical/horizontal pixel size of the detector and the magnification before and after visible light conversion. Cross-sections that are orthogonal to the human body axis are often used for diagnosis in medical X-ray CT scanners, but the cross-sections for the three intersecting directions are in most cases equally important

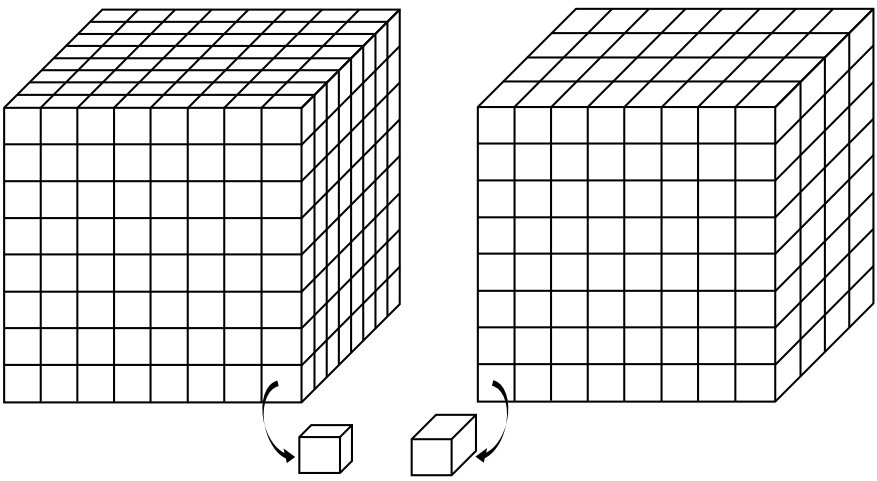

(a) 3D image that consists of isotropic voxels (b) 3D image that consists of anisotropic voxels

Fig. 7.1 Schematic showing the structure of a 3D image; **a** and **b** have an equivalent field of view for the image and horizontal/vertical voxel size in the front side with only the back-facing voxel length varying between the two

in industrial X-ray scanners and synchrotron radiation X-ray tomography. For these reasons, isotropic voxels have become necessary. The areas shown by images in all directions are assessed using *multi-planar reconstructions* (*MPR*) shown in Fig. 7.2.

Image file formats include stacks of 2D images in general formats, like TIFF, BMP, or JPEG, or DICOM, which is a standard format used in medical imaging.

Images obtained by X-ray tomography primarily use 16-bit ($2^{16} = 65{,}536$ gradations), 12-bit ($2^{12} = 4{,}096$ gradations), and 8-bit ($2^8 = 256$ gradations) bit-depth parameters. For example, the reconstructed linear absorption coefficient distributions in absorption contrast tomography are expressed in a *grayscale* such as 8-bit.

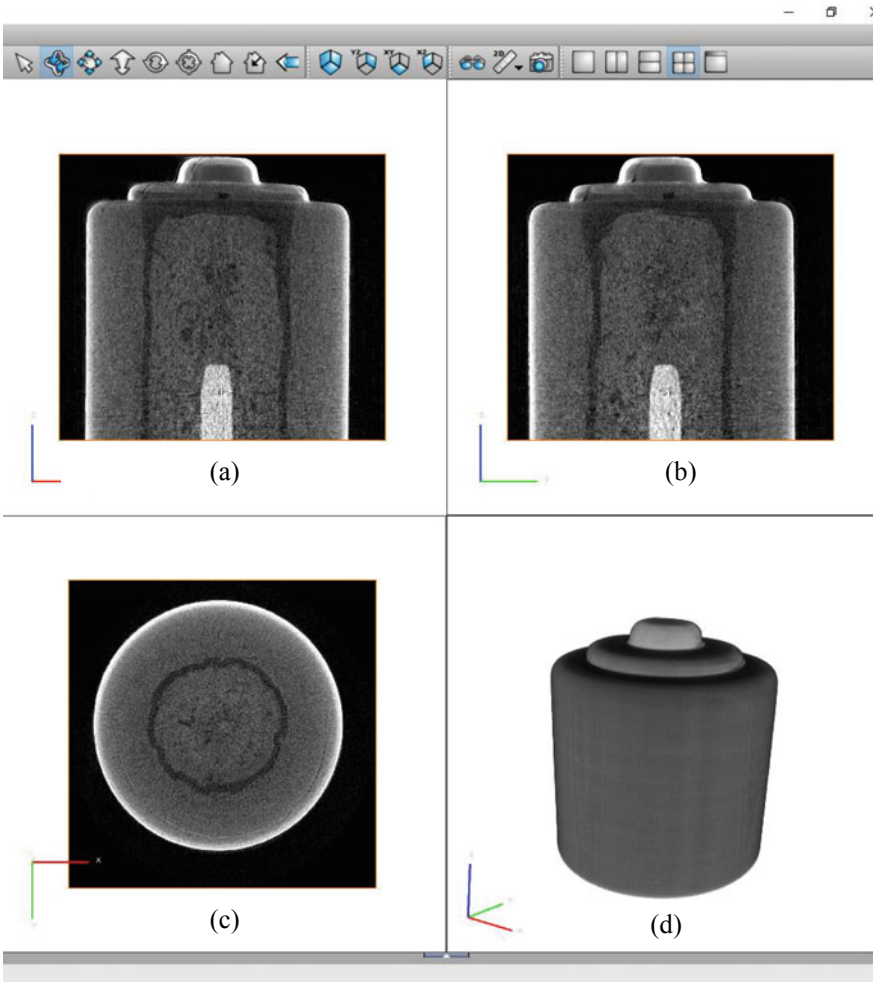

Fig. 7.2 Example of an MPR display of a 3D image of a battery; **a** x–z cross section, **b** y–z cross section, **c** x–y cross section, and **d** 3D image

Furthermore, distributions of the amounts measured by methods like phase-contrast tomography and various applied imaging methods are displayed. Figure 7.3 images a sample whose linear absorption coefficient gradually changes with distance from the center and which is shown with an 8-bit grayscale ranging from white (gray value of 255) to black (gray value of 0). Furthermore, Fig. 7.3d shows a *binarization* where a given *gray value* was set as a *threshold value*. This is, so to speak, a 1-bit black and white image that is used for structure size and morphology assessments. A decreased bit count of a 3D image reduces the amount of information but also reduces the amount of data, making handling easier. For example, an 8-bit 2,048 × 2,048-pixel image requires 4 MB of data but this doubled to 8 MB with a 16-bit

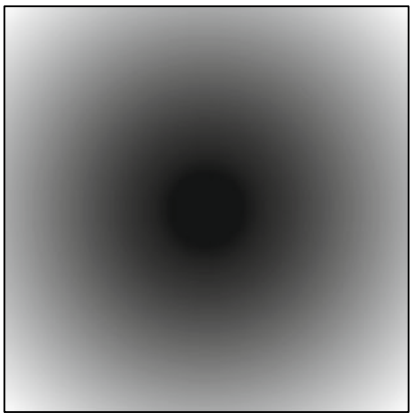

(a) Distribution of linear absorption coefficient in a substance

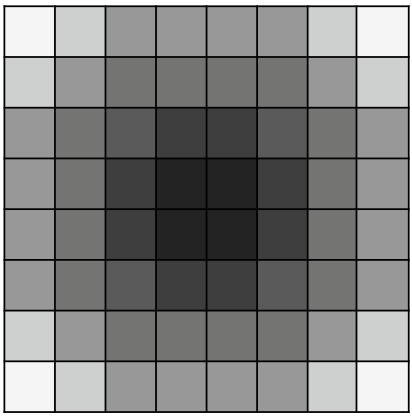

(b) 8-bit digital image that has been converted from (a)

234	215	205	192	192	205	215	234
215	187	168	143	143	168	187	215
205	168	80	35	35	80	168	205
192	143	35	10	10	35	143	192
192	143	35	10	10	35	143	192
205	168	80	35	35	80	168	205
215	187	168	143	143	168	187	215
234	199	215	192	192	205	215	234

(c) Grey value distribution for (b)

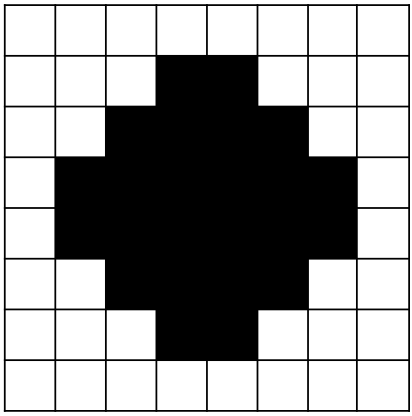

(d) Image obtained by binarizing (b) with a threshold value of 150

Fig. 7.3 Pixel display of a sample with a linear absorption coefficient gradient and schematics, which show its gray value distribution **a** is the distribution of linear absorption coefficient in a substance; **b** is an 8-bit digital image that has been converted from **a**; **c** is grey value distribution for **b**; and **d** is an image obtained by binarizing **b** with a threshold value of 150

image. Sufficient results can be obtained with an 8-bit depth if the imaging objective is only to display the distributions of numerous structures. Meanwhile, images with a larger bit depth (e.g. 16-bit) should be used when it is necessary to express differences in pixel values over 100 times larger, when there are many structures to be distinguished, or when a given structure has a gray value distribution and needs to be visualized. Thus, this should be determined on a case-by-case basis. In addition to these black-and-white or *binary images*, 3D images can also display multiple scalar quantities or vector values. For example, color images with intensities for the three RGB (red, green, blue) components can be displayed as well.

Chapter 4 discussed various types of noise such as photon noise that is unavoidable with X-ray tomography. Many artifacts are also unavoidable (discussed later). For these reasons, the grayscale range of 3D images as captured often has default settings in image reconstruction software that cover an unnecessarily-wide range of linear absorption coefficients, such as setting the maximum and minimum values of the linear absorption coefficients as the upper and lower edges, respectively. With this in mind, this must be changed to a grayscale range that corresponds to the linear absorption coefficients of multiple internal structures to be observed, as shown in Fig. 7.4. Furthermore, the bit count should be simultaneously reduced as necessary, as shown in Fig. 7.4. For example, a clear 3D image can be obtained when there are multiple structures present in a sample by setting the structure A with the lowest gray value as black (0 for an 8-bit gray value) and structure B with the highest gray value as white (255 for an 8-bit gray value). However, visualizing the gray value distributions of structures A or B requires having the observed gray value distribution fit inside an 8-bit gray value range. For this reason, it is not uncommon to use different gray value ranges for each structure to be analyzed. In either case, the basic principle is to look at the 3D image and assess it while constantly checking which gray values correspond with each of the internal structures that can be determined.

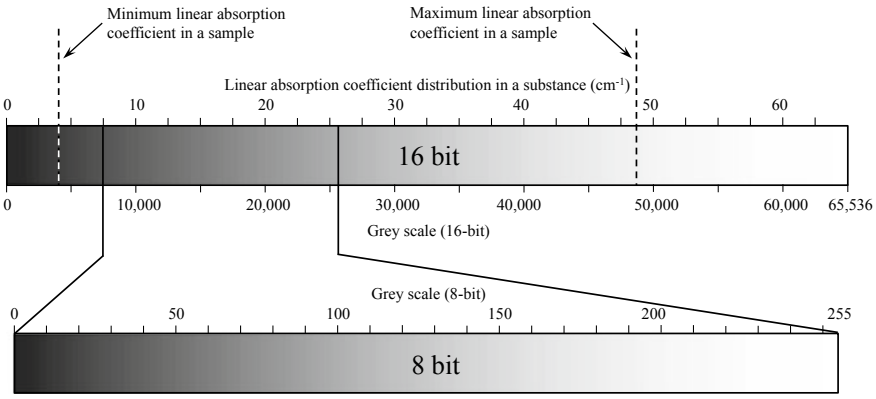

Fig. 7.4 Transformation from a 16-bit to 8-bit image, and the simultaneous change in gray-scale range

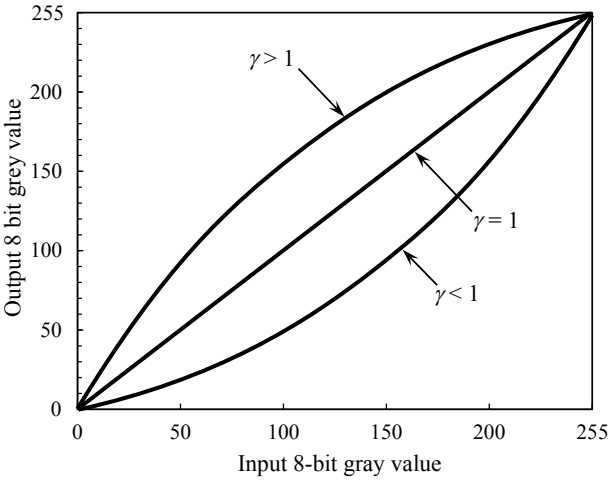

Fig. 7.5 Gray-level transformation function used for the gamma correction. Gray-level transformations for three different gamma values are shown

Incidentally, the transformation of the grayscale range usually follows a linear relationship. However, non-linear *gray-level transformation functions* such as those shown in Figs. 7.5 and 7.6 can also be used as necessary. Representative examples include the *gamma correction* shown below. The relationship between the input gray value g_{n} and output gray value g_{out} is as follows:

$$g_{\mathrm{out}} = g_{\max}\left(\frac{g_{\mathrm{in}}}{g_{\max}}\right)^{\frac{1}{\gamma}} \tag{7.1}$$

Here, $g_{\max}$ is the maximum gray value. The gray-level transformation function becomes concave in the upward direction as shown in Fig. 7.5 when γ is greater than 1. In this case, the output image becomes brighter overall, with the gray value differences in the brighter areas becoming smaller, and the gray value differences in the darker areas becoming greater. The gray-level transformation function becomes concave in the downward direction when γ is less than 1 and the gray value differences in the brighter areas become highlighted. Furthermore, an S-shape gray-level transformation function shown in Fig. 7.6a increases the contrast of low-contrast structures in the intermediate gray areas, making them easier to see, as shown in Fig. 7.6c.

Figure 7.7a shows a cross-sectional visualization of aluminum cast alloy microstructures using X-ray tomography. This figure is an 8-bit image that has been converted from a 16-bit image. Furthermore, Fig. 7.7b is the gray value histogram after 8-bit conversion. This sample includes gray-colored pores dispersed in the aluminum matrix (hydrogen interior: gray value of 0), intermetallic compounds that include iron (gray value of 255), and silicon particles whose gray values are close to

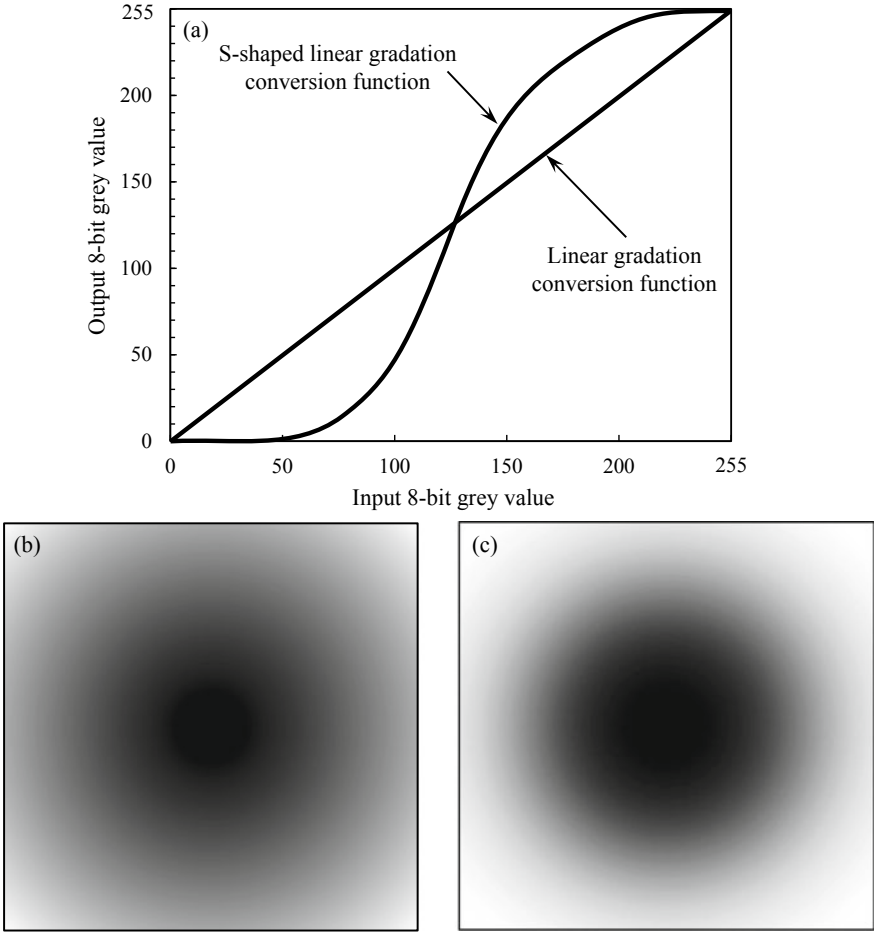

Fig. 7.6 Transformation of the image shown in Fig. 7.3. **a** using a non-linear gray-level transformation function; **b** is the original image and **c** is the image after transformation

aluminum. The pores can be clearly distinguished in the gray value histogram, but the other phases are not visible as peaks in the gray value histogram. It is extremely important to look at the obtained imaged in conjunction with the histogram, identify where the structures of interest fall on the gray value histogram, and pre-emptively investigate how to express those structures within the 3D image.

Changing the linear absorption coefficient range covered in a 3D image obtained by X-ray tomography and performing filtering operations on it are conducted routinely. Care must also be taken when handling these types of images. Careful consideration must be afforded to the cutting/pasting of images and processing only one section of an image, as well as to comprehensive secondary processing procedures such as nonlinear gray-level transformations. For example, if conducting a

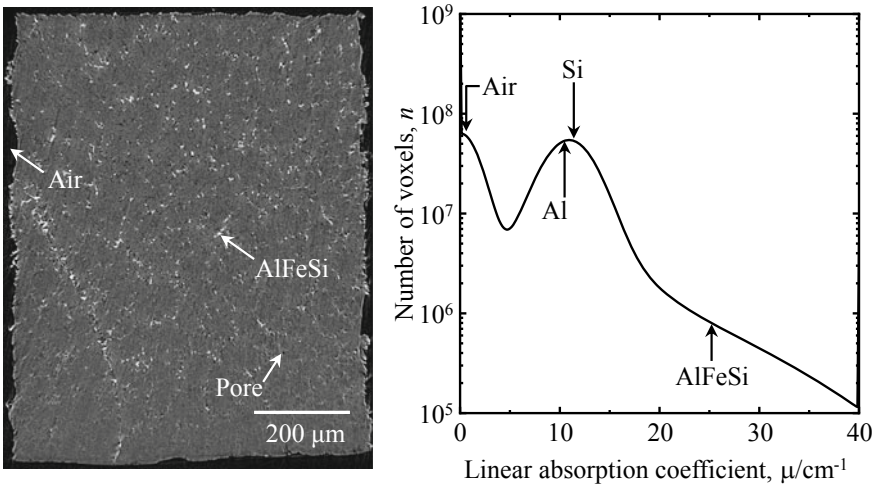

(a) Cross-section

(b) Histogram of pixel value for the whole 3D image

Fig. 7.7 **a** Cross-section image of Al-7% Si aluminum cast alloy using X-ray tomography. The imaging beamline BL20XU at SPring-8 was used and imaging was conducted with an X-ray energy of 20 keV; **b** histogram of gray value following 8bit conversion

gray-level transformation, the function used should be clearly stated, and the purpose and procedures used in this processing should be verifiable by a third party. The reason for this is that unexpected data processing may be perceived as a breach of research ethics by a researcher and of data manipulation by an engineer. Processing which changes the results derived from an image is not in the least acceptable. This strikes at the core of the trust and reliability that form the basis of science and technology. Scientists should apply the foundational knowledge learned from this book and proceed carefully and humbly with the analysis of 3D images, so that they may not, in their haste, whether intentionally or otherwise, swear black is white in the interpretation of the data.

7.2 Examination of 3D Images

The quality of 3D images is discussed before delving into image examination methods. The term “image quality” is not defined even in standards such as the Japanese Industrial Standards (JIS B7442: 2013), which stipulate the specialist terminology relating to industrial X-ray CT scanners [1]. Definitions relating to this term are also not included in the medical radiation terminology list (updated edition in 2012) relating to medical X-ray tomography; the first edition was published far earlier in 1991 in Japan [2]. The medical image engineering handbook issued in

2012 states, “the definition of image quality is ambiguous, and has been an ongoing issue of investigation.” [3] The perspective of some is that “image quality = resolution” but this is not entirely correct. The most general understanding of image quality is one that involves considerations of spatial resolution, detectability, noise, contrast, and artifacts. Each of these individual factors should be quantitatively assessed with methods that can be reproduced using objective measures. This chapter will look at these factors in order. Using the term “image quality” to express these elements, these individual factors will be comprehensively assessed with some degree of subjectivity, considering the objectives and significance of the 3D images used in research and development.

After measuring with X-ray tomography, image reconstruction of either a single cross-section or the entire data is conducted using one of the image reconstruction methods discussed in Chap. 3. The first step is to visually examine the quality of the 3D image, checking whether it requires re-measurement or whether there are any artifact-related issues (discussed later in Sect. 7.6). If the imaging is deemed to have been unsuccessful due to some unexpected reason, this is investigated and the measurement must be repeated. As detailed in Sect. 3.2.1, either investigating the sinogram or re-confirming the obtained transmission image stack as a fast-forwarded video is effective at this stage. The latter can likely be completed with built-in software in the device if it is an industrial X-ray CT scanner. Furthermore, if imaging was conducted using X-ray tomography at a synchrotron radiation facility, it can be completed via the image-processing features of the software that controls the CCD or sCMOS camera and acquires the images [4] or via software released by the beamline in the synchrotron radiation facility [5]. Similar assessments can be conducted with general image processing software when these cannot be used. For example, the image processing software ImageJ can easily conduct the confirmation of transmission images if the images are imported in the form of a TIFF-image stack [6]. Figure 7.8 shows an example of this confirmation process.

Other simple methods for checking for image quality deterioration involve comparisons between 0° and 180° transmission images. The 0° and 180° images will be the same when the range for transmission image acquisition is 0° to 180°. The only differences are that the image is flipped horizontally with regard to the rotational axis and the imaged time is shifted by almost exactly a single X-ray tomography imaging duration. The former can be used for the assessment of system alignment, such as the inclination between the rotation and detector axes and the horizontal shift in the rotation axis from the center of the detector. The latter can also be used to determine the amount of sample drift and deformation that occurred during an imaging period. A schematic of this is shown in Fig. 7.9. Slow sample movements due to factors such as the thermal expansion, plastic deformation, and creep deformation of the sample or sample holder are difficult to detect from visual inspections of the sinogram or transmission image video. However, this can be clearly yet simply determined with comparisons between the 0° and 180° transmission images.

A summary of the representative issues that occur during imaging is shown in Table 7.1. The primary methods, which can investigate the causes of these issues are also shown in Table 7.1. These methods should be used to troubleshoot these issues.

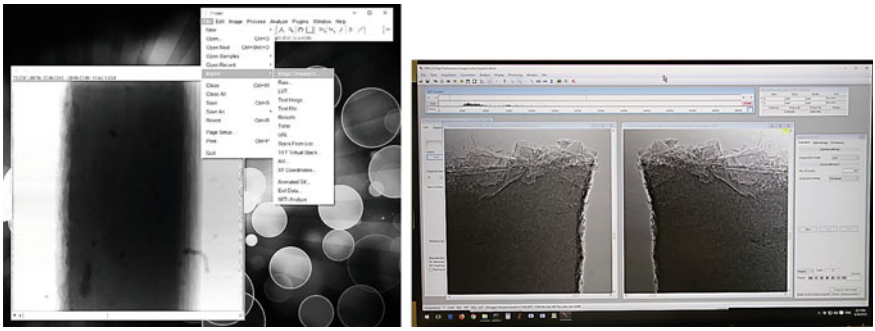

(a) Checking a transmission image using ImageJ

(b) Confirmation of transmission images in a synchrotron radiation facility

Fig. 7.8 **a** Screenshot of a display where transmission images are confirmed using a fast-forward video in ImageJ; **b** Shows an experiment image at the beamline BL20XU in SPring-8. Comparisons between 0° and 180° transmission images are conducted using the Hamamatsu Photonics software HiPic following measurements with X-ray tomography

7.3 Noise

As detailed in Sect. 4.4.1, noise is caused by various factors during X-ray imaging. Noise is unavoidable with 3D images measured by X-rays. The quantitative determination of noise is first necessary for its effective handling during X-ray tomography measurements, image processing, and image analysis.

7.3.1 Standard Deviation

The simplest way to assess noise is to calculate the *standard deviation* of the gray values in the 3D image. This is also referred to as *RMS granularity*. The standard deviation *SD* in a 3D image with n pixels is expressed as follows:

$$SD = \sqrt{\frac{1}{n}\sum_{i=1}^{n}(g_i - \bar{g})^2} \tag{7.2}$$

Here, g_i is the gray value of the ith pixel and $\bar{g}$ is the average gray value of all pixels. The normalized version of this, referred to as the *normalized standard deviation NSD*, is also used for noise assessment.

$$NSD = \frac{1}{\bar{g}}\sqrt{\frac{1}{n}\sum_{i=1}^{n}(g_i - \bar{g})^2} \tag{7.3}$$

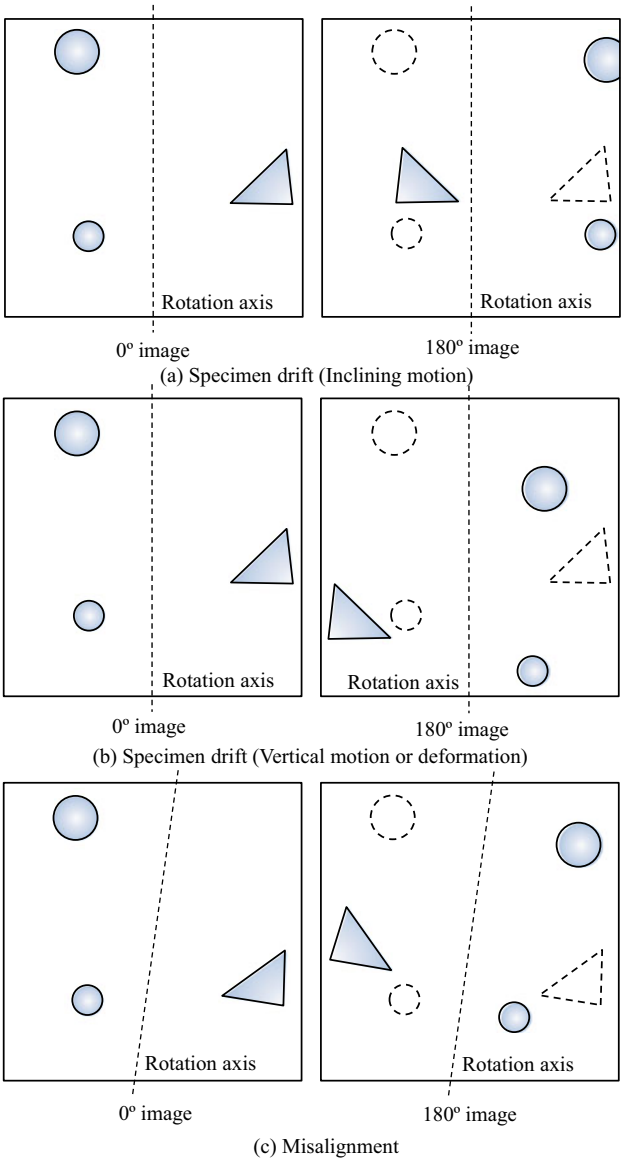

Fig. 7.9 Schematic showing the determination of the causes for decreased image quality using comparisons of 0º and 180º transmission images; **a** and **b** show deformation or vertical/horizontal movement of the sample or its supporting holder; **c** shows a case of misalignment between the rotation axis of the sample rotation stage and the detector. Normal conditions are when the rotation angle is vertical and when the same structures in the 0° and 180° images are symmetrical with respect to the rotation axis

Table 7.1 Representative issues that occur during imaging, their types, and methods for investigating its causes. Issues that arise in both industrial-use X-ray CT (ICT) and synchrotron radiation X-ray tomography (SRCT) are summarized. SRCT and ICT in the table each refer to synchrotron radiation X-ray tomography and industrial-use X-ray CT, respectively

Trouble	Type	Confirmation method	Associated technique
Shortage of spatial resolution	Image quality	Spatial resolution measurement in a 3D image	All
High noise level	Image quality	S/N ratio measurement in a 3D image	All
Shortage in flux	Image quality	S/N ratio measurement in a 3D image	All
Poor contrast	Image quality	Contrast measurement in a 3D image	All
Eccentricity and surface runout of a rotation stage	Image quality	Spatial resolution measurement in a 3D image	Mainly SRCT
Intensity fluctuation of an Xray beam	Image quality	Sinogram, movie of transmission images, etc.	Mainly SRCT
Nonuniformity and speckle noise of an X-ray beam	Image quality	Transmission image	Mainly SRCT
Misalignment	Artifact	Transmission image (Comparison of 0° and 180° images)	SRCT
Missing wedge of information (Angular limitation)	Artifact	Sinogram, movie of transmission images, etc.	Mainly SRCT
Sample drift	Artifact	Transmission image (Comparison of 0° and 180° images)	All
Sample deformation/change	Artifact	Transmission image (Comparison of 0° and 180° images)	All
Protrusion of a sample from a field of view	Artifact	3D reconstructed image	All
Beam hardening	Artifact	Reconstructed image (Virtual cross section)	Mainly ICT
Ring artifact	Artifact	Reconstructed image (Virtual cross section)	All
Metal artifact	Artifact	Reconstructed image (Virtual cross section)	All

(continued)

Table 7.1 (continued)

Trouble	Type	Confirmation method	Associated technique
Scattering artifact	Artifact/image quality	S/N ratio measurement in a 3D image, etc.	All
Undersampling	Artifact	Reconstructed image (Virtual cross section)	All
Corn beam artifact	Artifact	Reconstructed image (Virtual cross section)	ICT
Deviation of a rotation axis	Artifact	Reconstructed image (Virtual cross section)	All
Deflection artifact	Artifact	Reconstructed image (Virtual cross section)	Mainly SRCT

The standard deviations of multiple 3D images with variable exposure times are measured as an example. Images that have too short of an exposure time will inevitably have a large amount of noise. The standard deviations of the images in Fig. 7.10a–d are written in the figures. The amount of noise can be effectively expressed by using the standard deviation. However, we can also easily imagine that assessments with only standard deviation would not be possible if the gray value distributions in areas other than the noise are different. Considering the two types of samples shown in Fig. 7.11, the 3D image of sample A has lower noise but larger fluctuations in the gray value of the internal structure, while the structure of sample B is relatively homogeneous but has a poor image S/N ratio. The standard deviations of the gray values in both cases are 13. As the average gray values for each are also 48.5, the normalized standard deviations are both the same (i.e., 0.27). In these cases, assessments using the noise power spectrum discussed in the next section are necessary.

7.3.2 Noise Power Spectrum

The *noise power spectrum* (*NPS*) was previously referred to as the *Weiner spectrum* (*WS*) but has been currently standardized to the former by International Electrotechnical Commission (IEC) stipulations [7].

A 2D Fourier transform $F(u, v)$ of the image $g(x, y)$ whose noise is to be assessed is defined by Eq. (3.5). The mathematical definition of the noise power spectrum *NPS* shown in two dimensions is set as the square of the absolute value of the Fourier transform, as shown in the following equation [8].

$$NPS(u,v) = \lim_{X,Y\to\infty} \frac{1}{XY} \left\langle \left| \int_{-X/2}^{X/2} \int_{-Y/2}^{Y/2} g(x,y) e^{-2\pi i(xu+yv)} dxdy \right|^2 \right\rangle \tag{7.4}$$

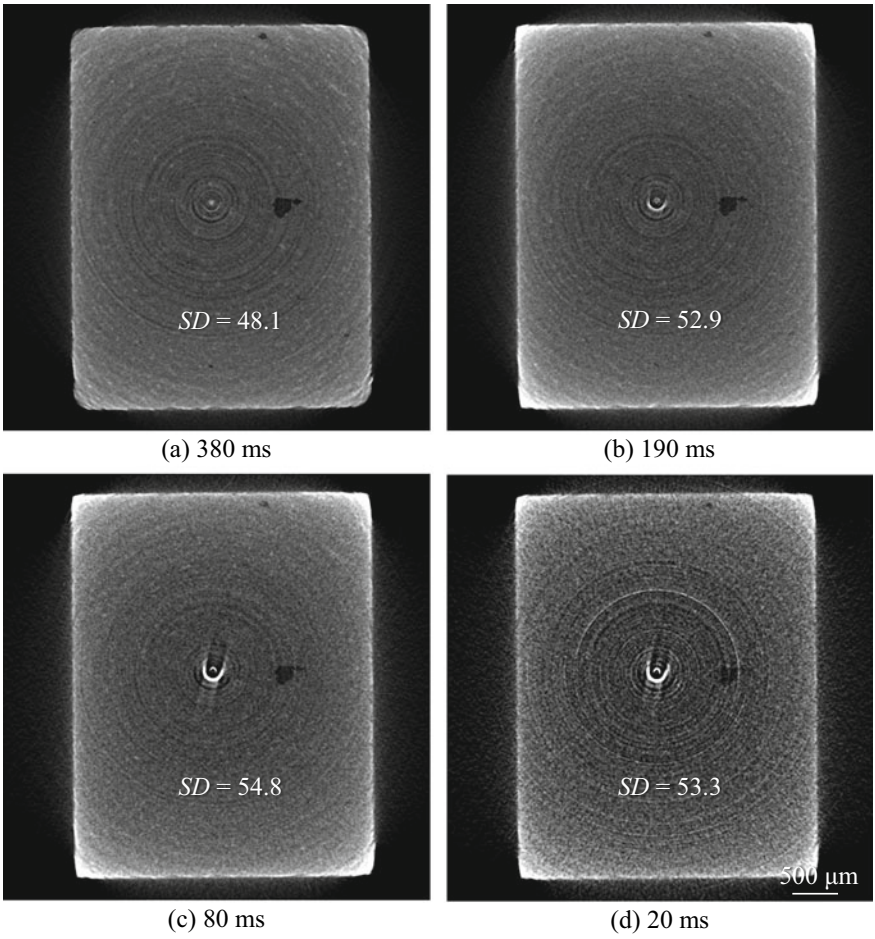

(a) 380 ms (b) 190 ms

(c) 80 ms (d) 20 ms

Fig. 7.10 Measurement results of noise due to standard deviation values produced when the exposure time in 3D imaging of the same sample was changed to induce different noise levels. Imaging conducted with the same device and imaging conditions are described in Sect. 7.6. **a**, **b**, **c** and **d** are 380, 190, 80 and 20 ms in exposure time, respectively

Here, X and Y are the sample sizes in the x and y directions. As such, the pixel sizes in the x and y directions are set as Δx and Δy and the pixel numbers are set as N_x and N_y, which yield $X = \Delta x N_x$ and $Y = \Delta y N_y$. The angle brackets in Eq. (7.4) signify the average of the infinite set of images. Furthermore, the noise power spectrum is a Fourier transform of an auto-correlation function. Equation (7.4) is effective only for cases of a Gaussian distribution where the average is 0; there are no images with an infinitely large size in reality [8]. As such, calculating the noise power spectrum in the region of interest within an actual image for a two-dimensional case yields the following expression:

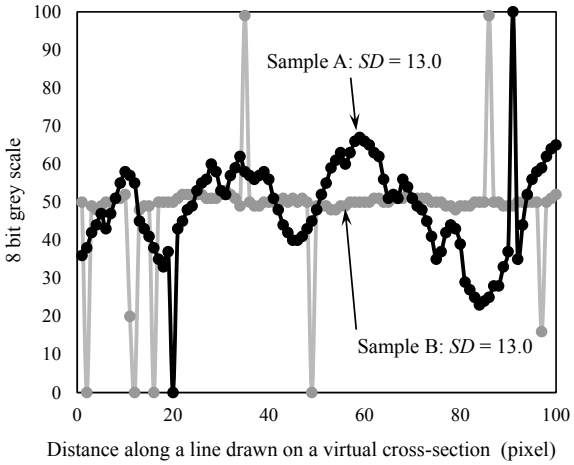

Fig. 7.11 Gray value distributions of two samples whose internal structure and microstructure are entirely different. A line segment is drawn across a given cross-section in a 3D image and the gray value histogram along that line segment is plotted. Sample A has large changes in X-ray absorption of the internal structure, but the image S/N ratio is favorable. Meanwhile, sample B has a relatively homogeneous internal structure, but the image has high amounts of noise

$$NPS_{2D}(u,v) = \frac{\Delta x \Delta y}{N_x N_y}\left\langle \left| DFT_{2D}\left\{ g(x,y) - \overline{g(x,y)} \right\} \right|^2 \right\rangle \tag{7.5}$$

Here, DFT refers to the discrete Fourier transform, which also appeared in Chap. 3. The above-mentioned equation applies not only to the (x, y) cross-section but the (y, z) and (z, x) cross-sections as well. Furthermore, the 3D noise power spectrum of a given region of interest is as follows:

$$NPS_{3D}(u,v,w) = \frac{\Delta x \Delta y \Delta z}{N_x' N_y' N_z'}\left\langle \left| DFT_{3D}\left\{ g(x,y,z) - \overline{g(x,y,z)} \right\} \right|^2 \right\rangle \tag{7.6}$$

Here, $\overline{g(x,y)}$ and $\overline{g(x,y,z)}$ are the average values and are subtracted in both equations for image trend elimination. Furthermore, N_x', N_y', and N_z' are the sizes of the region of interest (pixel number). The 1D noise power spectrum typically takes the average of *NPS* in the same spatial frequency (circumference of each concentric circle) of the 2D noise power spectrum to determine the spatial frequency distribution of the *NPS*.

$$NPS_{1D}(\omega) = \int_0^{2\pi} NPS_{2D}(\omega,\theta)d\theta \tag{7.7}$$

Here, the angular wave frequency is set as ω, and the Cartesian coordinates were transformed to polar coordinates (ω, θ).

Measurement examples of noise power spectra with different dimensions are shown in Fig. 7.12. The intuitive 1D noise power spectrum is frequently used. Regardless of the dimension in which assessments are conducted, multiple regions of interest must be taken and assessed by taking their averages. The measurement error e_{NPS} when taking the average *NPS* in an m number of regions is as follows [9].

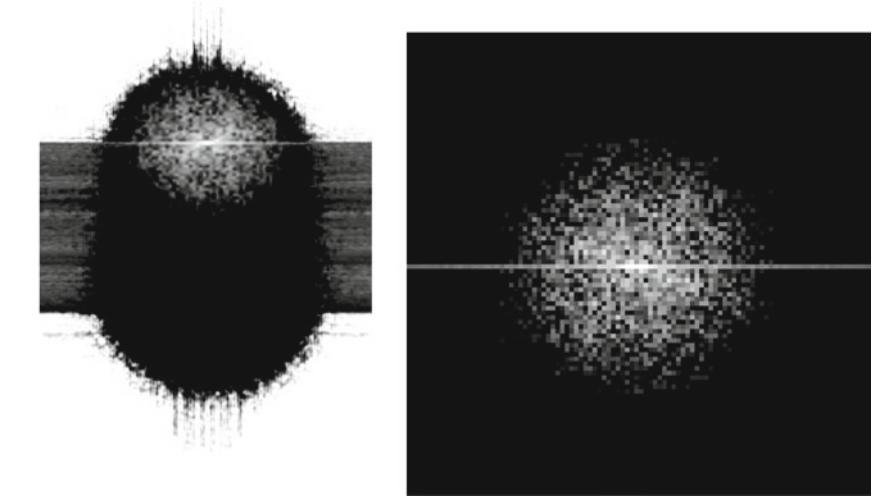

(a) Display in 3D (b) Display in 2D

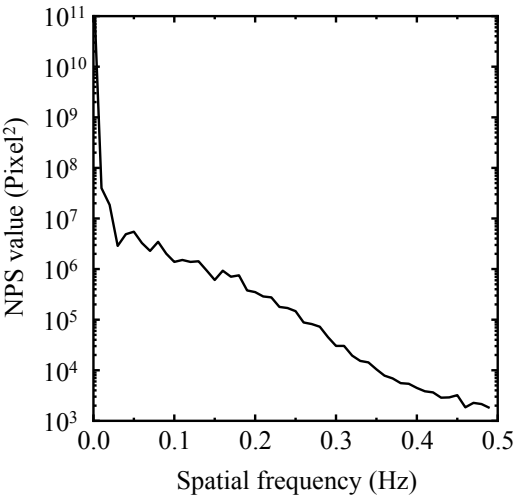

(c) Display in 1D

Fig. 7.12 Noise power spectrum of the 3D image shown in Fig. 7.10 **a** depicted in 1, 2, and 3 dimensions. **a** and **b** are displays in 3D and 2D, respectively. The 1D data in **c** (1D) is the data in **b** averaged in the circumferential direction

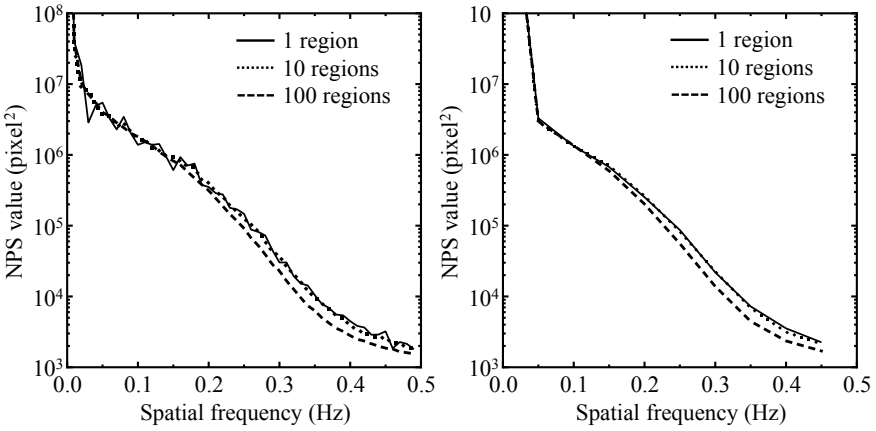

Fig. 7.13 The 1D noise power spectrum in Fig. 7.12 where measurements were made with varying sampling region numbers; **a** is the raw data and **b** is the data after a 5-section moving average was applied

$$e_{NPS} = \sqrt{\frac{1}{m}} NPS \tag{7.8}$$

Thus, a considerably large amount of sampling must be conducted to minimize errors. For example, the error drops to 1/10 after taking the averages of 100 regions of data. Figure 7.13 shows a 1D noise power spectrum with changes to the sampling number. Multiple regions of interest in a single image, must be measured, and several image sets must be prepared for a single sample to minimize error. Figure 7.13 shows the result of applying a 5-section moving average on data. These types of data processing are occasionally conducted to capture overall trends. Even measurements in a single region are capable of giving a picture of overall trends using the moving average, but they are inaccurate compared with measurements using 100 regions.

Figure 7.14 shows a 1D noise power spectrum of an image that was reconstructed with filtered back projection following the application of various reconstruction filters on projection data of aluminum-copper alloys in Figs. 3.27 and 3.28. The vertical and horizontal axes of Fig. 7.13 each show the extent of noise and spatial frequency. Although this image was measured using synchrotron radiation, noise ranging from coarse noise with low spatial frequency to fine noise with high spatial frequency is distributed in the image. Among these, filters with high spatial resolution capabilities like the Ram-Lak filter and the Shepp-Logan filter result in increased noise across a wide-ranging spatial frequency range. Meanwhile, filters with relatively low spatial resolution functionality such as the Hamming filter, Hann filter, and Parzen filter show considerably low noise.

The above-mentioned *NPS* calculations are relatively straightforward when using package software such as ImageJ or MATLAB. ImageJ also has a plug-in for NPS

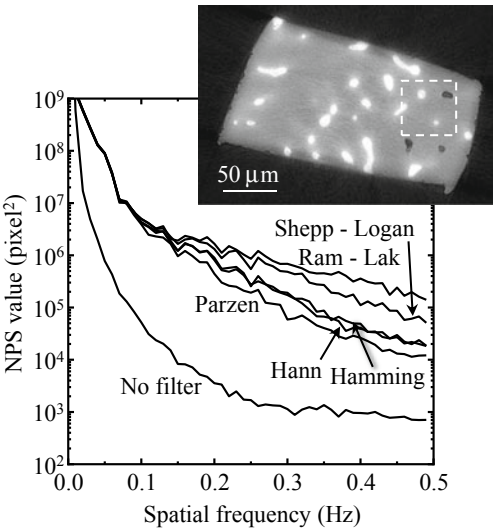

Fig. 7.14 1D noise power spectrum of a 2D image used for reconstruction filter assessments in Figs. 3.27 and 3.28 in Chap. 3. The noise differences due to the reconstruction filter can be compared. Measurements were conducted in the white-framed region shown in the photograph

calculations [10]. Simple calculations can still be conducted even if one does not have much experience using this type of analysis software if existing software such as CT image calculation programs released by the Japanese Society for CT Technology is used [10]. Software from the Japanese Society for CT Technology also includes MTF calculation functionalities (discussed later). These include trial versions for non-members mentioned in the reference, which allow for many more functionalities once becoming a member of the society [11].

7.4 Contrast

7.4.1 Basic Concepts

As mentioned in the introduction, device characteristics must be assessed in medical X-ray CT scanners through the image quality of 3D images. A standardized reference referred to as a phantom is used in these cases [12]. Measuring these allows for the assessment of image quality (including contrast) to determine performance changes in the device over time, daily. With regard to contrast, a term referred to as contrast resolution is stipulated in the Japanese Industrial Standards, which includes a list of terms for industrial X-ray CT devices. According to this, contrast resolution refers to the following: "the difference in industrial CT values (average) between a given section and its background which are at the limit of detection, taking into account the noise in a concentration resolution image" [1]. Noise has a large influence when the contrast between the background and observation subject is low. This is because the X-ray sources, detectors, and reconstruction functions appear similar in all the

hospitals, particularly in medical X-ray CT scanners. Specifically, assessments are conducted using the standard deviation and noise power spectrum discussed in the previous section, as well as the *contrast-to-noise ratio*. In this manner, contrast is assessed as an index that quantitatively describes the visual impressions when looking at the same section of a human body. There are multiple definitions for the contrast-to-noise ratio; please refer to the works cited for further information [13].

In contrast, it is important to conduct image quality assessments on all 3D images obtained using a diverse set of materials and sample sizes with industrial X-ray CT scanners and synchrotron radiation X-ray tomography. Suitable image quality assessments allow researchers to determine whether the internal structure to be observed is sufficiently reflected in the obtained 3D image and where the observable limits are in terms of size or contrast.

Image quality assessments handle images that vary greatly by X-ray source, detector, reconstruction method, and their various associated conditions. The basic principles for obtaining contrast in these cases not only involve differences in linear absorption coefficients obtained during absorption contrast tomography but the various methods discussed in Sect. 2.2 or Chap. 5. With this in mind, it has been the author's experience that assessments of noise, artifacts, and contrast should be conducted independently for industrial X-ray CT scanners and synchrotron radiation X-ray tomography. Furthermore, unlike with medical X-ray CT scanners, where visual assessments are the fundamental component, industrial X-ray CT scanners and synchrotron radiation X-ray tomography often seek volume rendering based on segmentation (discussed in Chap. 8) and quantitative assessment and measurement on morphology and size. Thus, the ultimate measure for contrast quality following the application of suitable filters (discussed in Chap. 8) involves whether the various phases and regions in the sample interior can be accurately segmented while removing noise and artifact effects. It is vital when applying industrial X-ray CT scanners and synchrotron radiation X-ray tomography for cutting and polishing samples to first conduct two-dimensional observations; these observations can be obtained using devices capable of easily acquiring a wealth of information on factors such as chemical composition at a higher spatial resolution (such as scanning electron microscopes). The existence and details of the structure to be observed should be understood as thoroughly as possible beforehand, as diverse samples will be observed with the limited spatial resolution and contrast of X-ray tomography.

7.4.2 Quantitative Assessment

There are several standard measures of contrast. One of these, referred to as the *Weber contrast* C_{W}, is as shown below:

$$C_W = \frac{g_f - g_m}{g_m} \tag{7.9}$$

Here, g_f and g_m refer to the gray values for the region/phase and the background, respectively, of the observation subject. The Weber contrast is suitable when a small region is dispersed in a homogeneous background. Furthermore, the *Michelson contrast* C_M is as shown below:

$$C_M = \frac{g_h - g_l}{g_h + g_l} \tag{7.10}$$

Here, g_h and g_l refer to the two regions of the observation subject, with the former having the high gray value and the latter having a lower gray value. Michelson contrast is suitable for cases where there are dark and light phases. Furthermore, Eq. (7.2) is used as RMS contrast when the image patterns are random and granular. Care must be taken in each case so that the gray value of the observation subject structure, rather than the noise, is used. The contrast measurement that is most suitable for the characteristics of the spatial distribution of the structure of interest in the sample should be selected among the many measurement methods available.

The Japanese Industrial Standards that define the terminology for industrial X-ray CT device state that Michelson contrast should be calculated based on the CT value of air (according to JIS, this refers to a gray value of an arbitrary scale) [1]. Care must be taken in these cases as this is not accurately calculated when the air or observation subject structure is set outside of the scale during the grayscale or bit depth conversions shown in Fig. 7.4.

7.5 Spatial Resolution

7.5.1 Fundamental Aspects

(1) Spatial Resolution as a Device and 3D Image Spatial Resolution

Spatial resolution is an index that relates whether two points in proximity to one another can be distinguished as two different points; it is stipulated as the minimal distance in which this distinction occurs [1]. Often, the spatial resolution of X-ray tomography devices is inferior to two-dimensional visualization devices commonly used in laboratories (e.g. scanning electron microscopes or transmission electron microscopes). For this reason, sometimes sample sizes and internal structures that are close to the effective spatial resolution are assessed in X-ray tomography. Thus, it is essential that the effective spatial resolutions obtained in the 3D imaging conducted by the reader are correctly determined.

As summarized in Table 7.2, the factor with the lowest accuracy among the diverse set of factors in X-ray tomography (e.g. X-ray source, sample rotation stage, X-ray focusing element in the case of the imaging optical system, and detector) acts as the rate-limiting element that dictates the maximum spatial resolution achievable by

Table 7.2 Major elements that can potentially constrain the spatial resolution in industrial-use X-ray CT scanners and synchrotron radiation X-ray tomography. The *sign refers to factors relating to the Nyquist frequency based on the sampling theorem

Elements	Factors
X-ray tube, etc.	Effective focal spot size
	Transmissivity (X-ray energy)
Imaging optical system Enlarged projection	Spatial resolution of an X-ray focusing device
	Magnification
	Illumination system
Sample rotation stage	Eccentricity and surface runout of a rotation stage
	Sample drift
Detector Fiber optics Optical lens	Effective pixel size*
	Various noise
	Scintillator thickness
	Scintillator stopping power
	Diffraction limit of visible light
Sample	Drift due to insufficient sample fixing
	Material deformation/transformation
Imaging condition	Flux (Exposure time)
	Rotation step*
Reconstruction	Reconstruction filter
	Incomplete dataset in cone beam reconstruction
	Filtering effects during phase retrieval process
Others	Various artifact
	Blurring due to Fresnel diffraction

an X-ray CT scanner. Additionally, this can be confirmed in Eq. (5.29) and (7.30). The spatial resolution is also greatly affected by the sample, imaging conditions, and various types of noise and artifacts. Intrinsically, the spatial resolution, which expresses performance as a system, should be assessed independently of the noise, artifacts, and imaging conditions, whose magnitude and type vary with different conditions. However, noise and artifacts can be said to be unavoidable with X-ray tomography. Furthermore, these can have an influence not only on image quality but also visualization success depending on the sample or imaging conditions. For these reasons, the spatial resolution should be calculated using the 3D images obtained under the imaging conditions and environment that can realistically be achieved; moreover, a device-/sample-/imaging condition-specific local spatial resolution in a given region of interest in the sample interior should be assessed.

There are multiple measures relating to spatial resolution in medical and industrial X-ray tomography and there may be some variation or even at times confusion in their definitions as in, for example, terms such as resolution, resolving power, spatial resolution, sharpness, or detectability. Some expressions specify the resolution and resolving power for images and spatial resolution for device specifications. However, for the previously mentioned reasons, this book systematically defines spatial resolution as the spatial resolution that can be measured for 3D images, which is the outcome of X-ray tomography. Furthermore, the term "detectability" must be accurately defined as a separate measure from spatial resolution.

Of the various conditions in Table 7.2, multiple factors relating to the devices have been discussed up until now in Chaps. 4 and 5. Unfortunately, however, the spatial resolution of industrial X-ray CT scanners is frequently not presented as the maximum spatial resolution in catalogs, etc. as part of comprehensive specifications based on the factors listed in Table 7.2. Often, the focal point size of the X-ray tube or the effective pixel size is shown instead of the spatial resolution or sometimes as the spatial resolution itself. As can be observed in the examples shown below, these often produce significant errors.

Figure 7.15 shows valuable data where the sample size varied in a Russian matryoshka-doll-like pattern, as shown in Fig. 7.15a, b, and where the sample was scanned at the same position and compared among two types of industrial X-ray CT scanners and Synchrotron radiation X-ray tomography (high-resolution imaging beamline BL20XU at SPring-8) [14]. The dashed line in Fig. 7.15c is the relationship between the pixel size and the spatial resolution, which is based on the sampling

(a) A nest of test jigs for spatial resolution measurement. The right cylinder was used for the measurement.

(b) After assembling three jigs shown in (a)

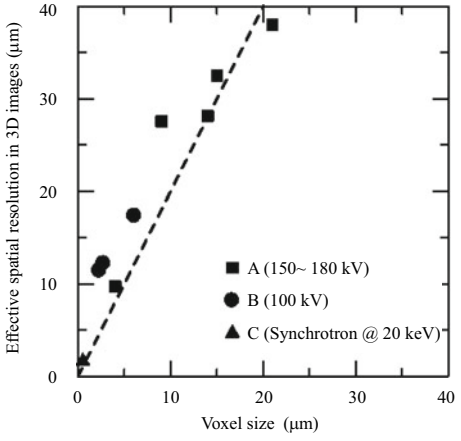

(c) Spatial resolution values of three X-ray CT scanners measured using the jigs shown in (a)

Fig. 7.15 The relationships between 3D pixel size and effective spatial resolution were measured and compared in nested test pieces shown in **a** and **b** using two types of industrial X-ray CT scanners (devices A and B) and the synchrotron radiation tomography instrument BL20XU at SPring-8 (device C) [14]. **c** shows the spatial resolution values of three X-ray CT scanners measured using the jigs shown in **a**. The dashed line in the figure expresses the sampling theorem

theorem discussed in the following section. Changing the pixel size in industrial X-ray CT scanners A and B changes the spatial resolution for each device in which the focal spot size of the X-ray tube does not constrain the spatial resolution. The measurement points for both industrial X-ray CT scanner A and synchrotron radiation X-ray tomography are mostly above the dashed line. This indicates that the spatial resolution is constrained by the Nyquist frequency based on the sampling theorem discussed in the following section. Meanwhile, the spatial resolution of industrial X-ray CT scanner B is lower than the level stipulated by the sampling theorem by a factor of 1.5–2.5. This signifies that a factor other than those marked with * in Table 7.2 controls the effective spatial resolution. Identifying the factor which constrains the spatial resolution in these cases and implementing suitable measures can result in considerable improvements to spatial resolution, which correspond to this difference.

Figure 7.16 uses the three types of devices in Fig. 7.15 and shows observations/comparisons of the same sample at the same positions while changing the pixel size. A more detailed structure is visualized as devices with higher spatial resolution

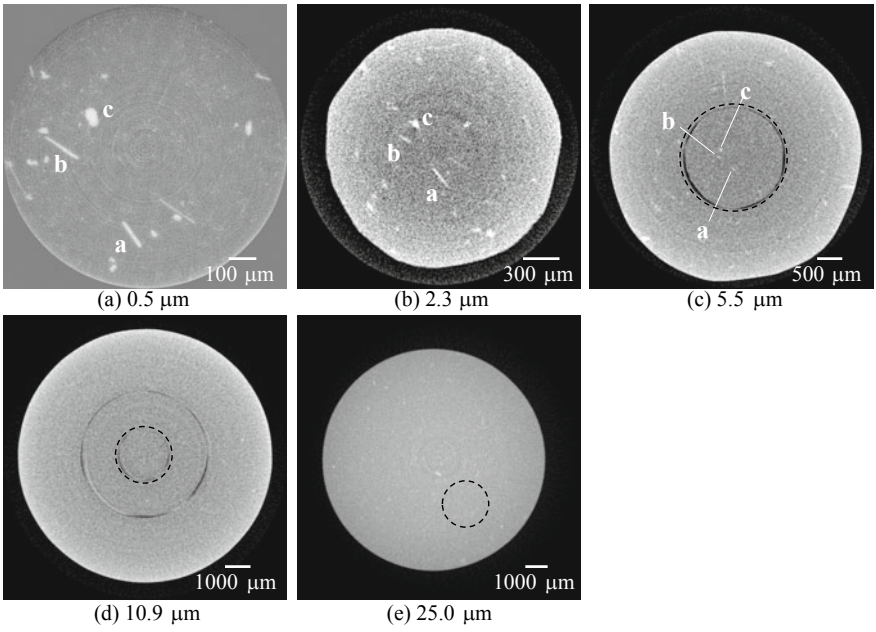

Fig. 7.16 Nested test pieces shown in the left side of Fig. 7.15 scanned at the same positions and with different voxel sizes using the two types of industrial X-ray CT scanners (devices A and B) and the synchrotron radiation tomography instrument BL20XU at SPring-8 (device C), referred to in Fig. 7.15 [14]. Device C was used for the pixel size of 0.5 μm in **a**; device B for 2.3, 5.5, and 10.9 μm in **b**, **c** and **d**, respectively; and device A for 25 μm in **e**. The **a** and **b** in the figure refer to the acicular Al_3Ti particles in the aluminum, and **c** refer to the TiB_2 particles. The dashed circles in (**c**–**e**) designate the same region in the sample shown in (**b**). Only (**a**) shows imaging of a region of interest in a portion of the sample shown in (**b**)

capabilities are used and when the pixel size becomes smaller in the same device (Fig. 7.16b–d). Structures that were clearly visible in Fig. 7.16b cannot be visualized at all in Fig. 7.16d, where the pixel size has increased by a factor of approximately 5. It is apparent that the sample size must be minimized to the extent possible and the sample must be placed as close to the X-ray tube as possible to acquire a sufficient spatial resolution. This is a frequently overlooked fact among industrial X-ray CT users.

The Fresnel diffraction of the X-ray and the Rayleigh diffraction limit, after the X-ray was converted to visible light, act as the bottlenecks for spatial resolution when improving the various conditions in Table 7.2 for projection-type X-ray tomography using a parallel beam. These stipulate the physical limits of spatial resolution, therefore, projection X-ray tomography cannot exceed a maximum spatial resolution of slightly less than 1 μm. Even with the example of synchrotron radiation X-ray tomography in Fig. 7.15, the effective spatial resolution is approximately 1 μm when the pixel size is approximately 0.5 μm; it is clear that the physical limits of spatial resolution have been reached.

(2) Sampling Theorem

Sampling in a 3D space in all x-, y-, and z-directions at a short periodicity is necessary for X-ray tomography to achieve a sufficiently small spatial resolution relative to the structure size to be observed in the sample. First, we consider this with a 1D image for simplicity. A 1D image is shown in Fig. 7.17a. The actual physical object is continuous even with observations with magnifications at the atomic level. Digital images are considered discrete expressions of continuous physical objects. Mapping a continuous function with a discrete function is referred to as *sampling*. The process of obtaining a digital image from a detector is multiplying a sampling function $s\,(x)$ by a primitive function $f\,(x)$, as shown in the following equation:

$$f_s(x) = f\,(x)s(x) \tag{7.11}$$

Here, $f_{\mathrm{s}}\,(x)$ is the sampled image and is as shown in Fig. 7.17e. The *sampling function* is also referred to as the *comb function*, taking the form of delta functions regularly spaced at a periodicity $\Delta\,x$, as shown in Fig. 7.17c.

$$s(x) = \sum_{n=-\infty}^{\infty} \delta(x - n\Delta x) \tag{7.12}$$

The pitch of this sequence of functions stipulates the spatial resolution. As shown in Fig. 7.17b, the Fourier transform of the primitive function $f\,(x)$ either has the spatial frequency components included in the original image below ν_c or is bandwidth limited. This ν_c is referred to as the *cutoff frequency*. Furthermore, the comb function is used for the Fourier transform of the sampling function $S\,(x)$, as shown in Fig. 7.17d:

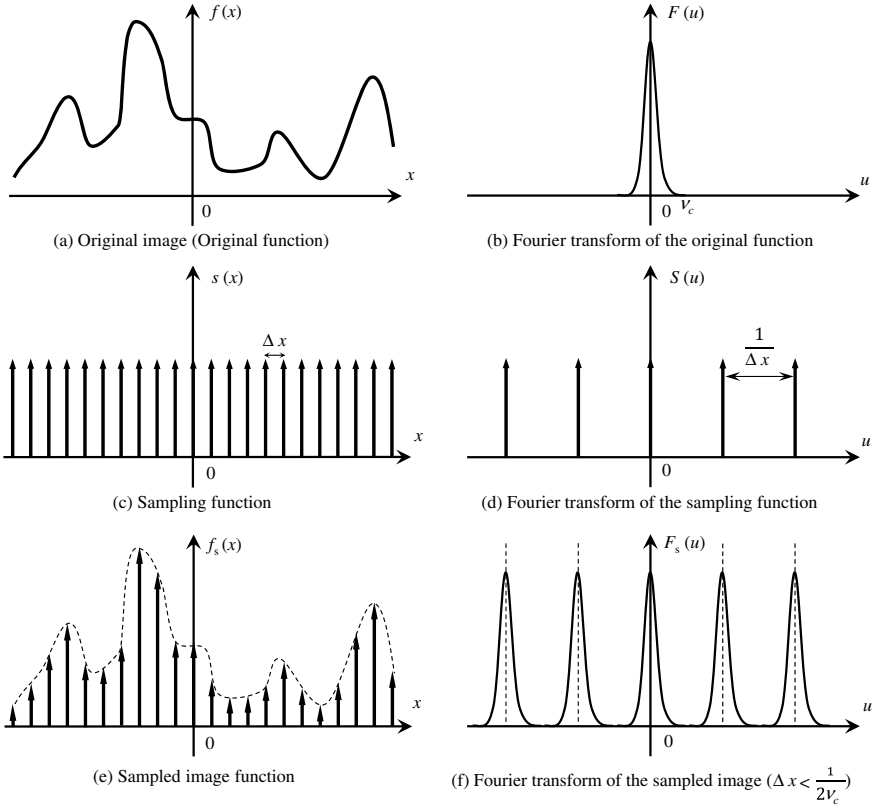

Fig. 7.17 Schematic of spectra in real space and frequency space when imaging a 1D image with a detector. The sampling function is an example of a delta function stipulated by the sampling pitch Δx determined by the pixel size of the detector; $\Delta x < \frac{1}{2v_c}$ (over-sampling) is satisfied in this case and the original image can be accurately reconstructed. **a** an original image; **b** Fourier transform of **a**; **c** sampling function; **d** Fourier transform of **c**; **e** sampled image function; and **f** Fourier transform of **e** ($\Delta x < 1/2v_c$)

$$S(x) = \frac{1}{\Delta x} \sum_{n=-\infty}^{\infty} \delta\left(u - \frac{n}{\Delta x}\right) \tag{7.13}$$

The multiplication operation on the sampling function in Eq. (7.11) is equivalent to convoluting the sampling function in the frequency space.

$$F_s(u) = F(u) * S(u) = \frac{1}{\Delta x} \sum_{n=-\infty}^{\infty} F\left(u - \frac{n}{\Delta x}\right) \tag{7.14}$$

In other words, $F(u)$, obtained by applying a Fourier transform on the primitive function as shown in Fig. 7.17f, can be periodically repeated by sampling it. The following rectangular function is used to extract the spectra of the original image from this.

$$H(u) = rect(u\Delta x) \tag{7.15}$$

A filtering process using this function in the frequency space produces an accurate Fourier transform of the original image.

$$F(u) = H(u)F_s(u) \tag{7.16}$$

Finally, an inverse Fourier transform of the equation shown above results in the following expression:

$$f(x) = \sum_{n=-\infty}^{\infty} f(n\Delta x)\mathrm{sinc}\left\{\frac{\pi}{\Delta x}(x - n\Delta x)\right\} \tag{7.17}$$

In other words, multiplying a *sinc* function to the images sampled at a period Δx and adding these reproduces the primitive function. This is referred to as the *sampling theorem*.

The primitive function cannot be successfully reproduced in Fig. 7.18b due to overlapping adjacent spectra even if filtering is conducted as shown in Eq. (7.16). This phenomenon is referred to as *aliasing*. Conditions where the sampling number is insufficient are referred to as *undersampling*. Aliasing artifacts (discussed later) appear on the image in these cases. Meanwhile, the spectra in Fig. 7.18c are sufficiently spaced apart; these conditions are referred to as *oversampling*. Figure 7.18a, where the *Nyquist frequency* f_{N} is half of the sampling frequency $1/\Delta x$ and $f_{\mathrm{N}} = \nu_c$ is satisfied, presents the optimal conditions for accurately conducting image reconstruction while controlling the amount of data.

$$f_N = \frac{1}{2\Delta x} \tag{7.18}$$

Therefore, the original image can be accurately restored when the maximum frequency component ν_c of the original image is known by sampling at an interval finer than double this value (i.e., $2\nu_c$). There are usually detailed multiscale structures (e.g. material microstructures) in a sample. As such, Eq. (7.16) can be stated in real terms as follows: "the spatial resolution necessary for imaging the internal structure to be observed should be recognized and measurements should be taken at a pitch that is half this value."

Figure 7.19 shows a 2D case. The concepts here are the same for this 2D case. In other words, the measurement pitches Δx and Δy for the two x- and y- directions are determined by the pixel size of the detector. In this case, Eq. (7.17) is expressed as follows:

$$f(x, y) = \sum_{n=-\infty}^{\infty}\sum_{m=-\infty}^{\infty} f(n\Delta x, m\Delta y)\mathrm{sinc}\left\{\frac{\pi}{\Delta x}(x - n\Delta x)\right\}\mathrm{sinc}\left\{\frac{\pi}{\Delta y}(y - m\Delta y)\right\} \tag{7.19}$$

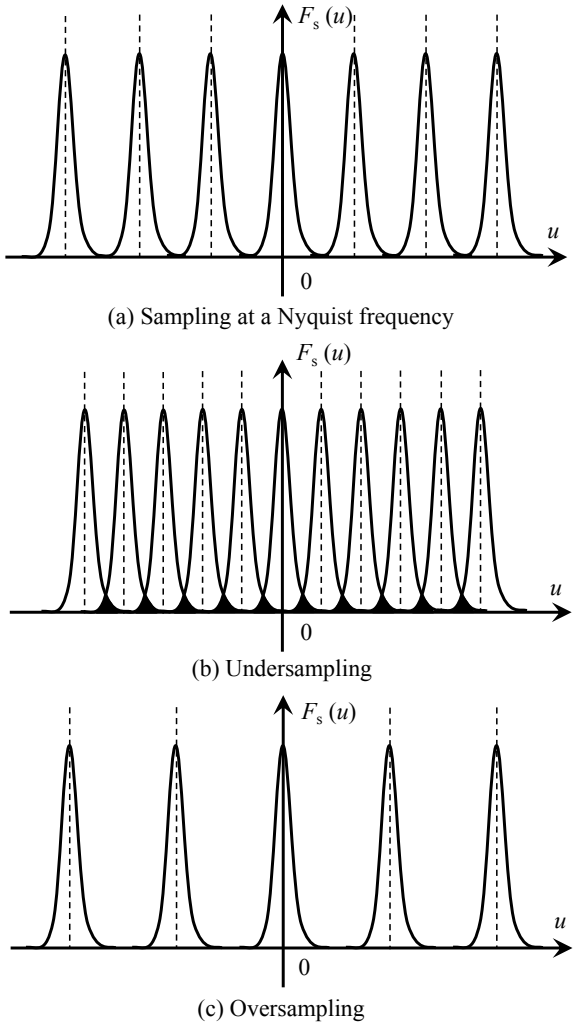

Fig. 7.18 A 1D image obtained from a detector and normalized, after which a Fourier transform was applied; the schematic shows three cases with different sampling frequencies. **a** is sampling at a Nyquist frequency; **b** is undersampling; and **c** is oversampling

As shown in Fig. 3.42a in Chap. 3, the rotation axis of the sample rotation stage is placed during actual X-ray tomography measurements so that it is perpendicular to the incident direction of the X-ray. The 2D detector is used to conduct continuous imaging of transmission images multiple times while rotating the sample by 180°, with this rotation axis at the center. Thus, with regard to the cylindrical coordinates (r, φ, z) corresponding to the rotation axis of the sample rotation stage, the effective pixel size of the detector must exceed the Nyquist frequency in the r- and z-directions, as well as the rotation step (interval expressed as distance) of the sample rotation stage in the φ direction. For example, the ideal spatial resolution in the φ direction at the edge of the field-of-view when conducting imaging of a total of M transmission images during 180° rotation with a field-of-view width and height of D are $\pi D/M$.

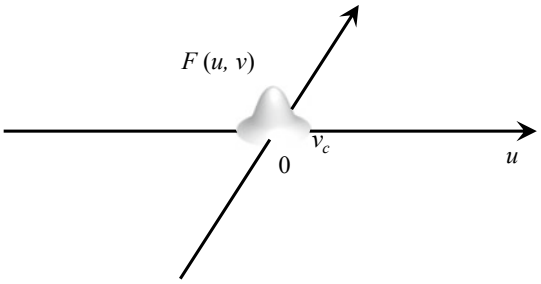

(a) Fourier transform of an original function

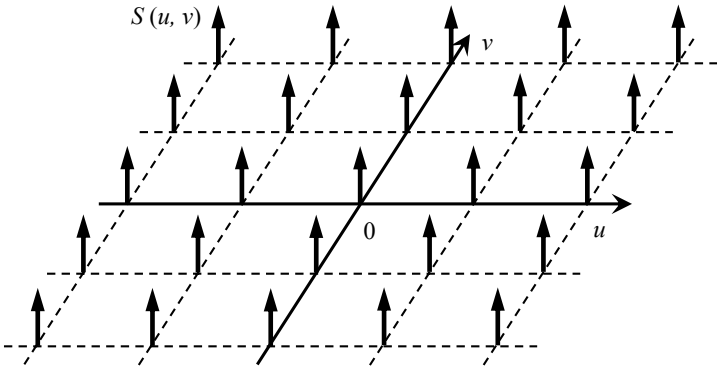

(b) Fourier transform of a sampling function

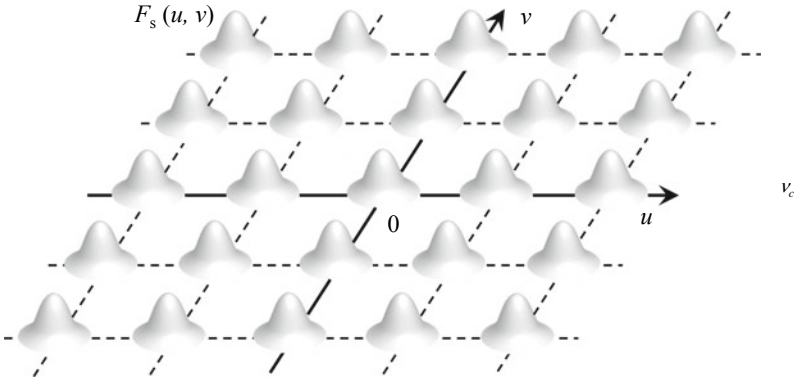

(c) Fourier transform of a sampled 2D image ($\Delta x, \Delta y < \frac{1}{2v_c}$)

Fig. 7.19 Schematic of spectra in frequency space when imaging was conducted using a 2D detector. The sampling function is a sequence of delta functions stipulated by the sampling pitches Δx and Δy, which are determined by the detector and pixel size; Δx, $\Delta y < \frac{1}{2v_c}$ (oversampling) is satisfied in this case and the original image can be accurately reconstructed. **a** is the Fourier transform of an original function; **b** is the Fourier transform of a sampling function; and **c** is the Fourier transform of a sampled 2D image (Δx, $\Delta y < 1/2v_c$)

The maximum spatial resolution value in the *r*- and *z*-directions when a detector with a pixel number of *N* in both the horizontal and vertical directions is used for measurement is $2D/N$. The selection of the number of pixels in a detector is not flexible in many cases. Thus, the number of projections becomes $\pi N/2$ if an isotropic spatial resolution is desired. However, the fact that various factors from the light source to the detector overlap and determine the effective spatial resolution has previously been discussed. Furthermore, the sample size is often smaller, to some extent, than the field-of-view size, therefore, the sampling pitch in the *r*-direction can be coarser than this based on the ratio between sample size and field-of-view size.

(3) Detectability

Spatial resolution and *detectability* are two completely different indices. Although detectability cannot be inferior to spatial resolution, the opposite is possible. In other words, detectability can be a value that is several times smaller than the pixel size, depending on the conditions. Detectability is largely influenced by spatial resolution, imaging methods and conditions, sample structure, and noise.

A schematic of this is shown in Fig. 7.20. Here, we consider the case of the 3D imaging of a material that includes 0.3–0.6-μm diameter particles and pores, as shown in Fig. 7.20a, with a 1-μm spatial resolution device/conditions. When the noise or artifact effects are low, the gray value of the pixels, in which such microstructures are embedded, changes, facilitating the discrimination and binarization of the pixels by employing the binarization shown in Fig. 7.20c. The noise/artifacts cannot be distinguished from the microstructure at this stage. However, as shown in Fig. 7.20d, the capability of detecting microstructures below the spatial resolution can be verified by repeating observations in the same location while growing this structure or by supplementing these with other observations/analysis methods. The detectability, in this case, is 0.27 μm when the maximum threshold was set as an 8-bit gray value of 240. This is 1/3 that of the spatial resolution. Thus, detectability is not only influenced by the structure size but also the microstructure to be detected and the linear absorption coefficient of the matrix. Positioning also plays a role in this as microstructures that are located between pixels are more difficult to detect than structures that are not; in other words, detectability is not homogeneous in a 3D image.

Improvements in microstructure detectability are considered achievable when black and white fringes, generated with refraction contrast imaging (discussed in Sect. 2.2.2 (2)), are utilized as the interfaces can be emphasized and the gray value of the microstructure can be significantly increased or decreased.

Detectability is difficult to directly measure experimentally unless special model samples are prepared. However, as mentioned above, researchers should investigate and be cognizant of the appropriate detectability level at each step of 3D image handling by attaining a deep understanding of the sample, basic imaging principles, internal and microstructure of the sample to be observed, imaging conditions, and the supplemental usage of confirmatory methods. This can minimize the erroneous loss of valuable information that may appear like noise at first glance through processes like filtering.

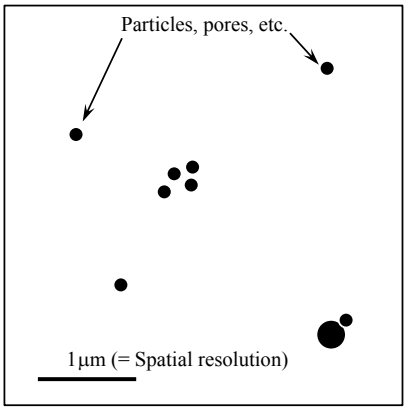

(a) Distribution in linear absorption coefficient at time, $t = t_1$

255	255	255	255	255	255	255	255
255	255	255	89	255	255	237	255
255	237	255	255	255	255	255	255
255	255	255	182	255	255	255	255
255	255	255	255	255	255	255	255
255	255	237	255	255	255	255	255
255	255	255	255	255	255	165	255
255	0	255	255	255	255	255	255

Noise

Noise

(b) 8-bit digital image of (a)

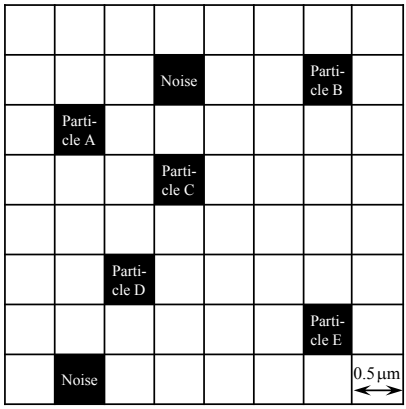

(c) After binarizing (b) with a threshold value of 240

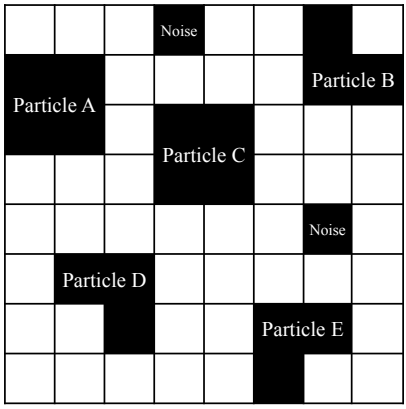

(d) Segmented 2D image at time, $t = t_2$ ($t_2 > t_1$)

Fig. 7.20 Schematic where 3D imaging was conducted on a material (gray value of 255) with microscale particles A–E (gray values of 165 to 237 in image **b**) show in **a** using a 1-μm spatial resolution (effective pixel size of 0.5 μm) setup; **b** is the obtained image, **c** is the binarized image, and **d** is a re-observation of the particles, which grew after a given period. Image **b** includes two points of noise, five microstructures, and its aggregates. Image **d** does not show noise in the positions in **b** and the microstructure has grown. For this reason, both structures exceed the spatial resolution and can be clearly identified

7.5.2 Spatial Resolution Assessment

(1) PSF, LSF, and ESF

A mathematical expression of the blur in an image taken by an X-ray CT scanner is the convolution of a non-blurred original image with an impulse response. The impulse response for an image is referred to as *the point spread function* (*PSF*). The spatial resolution takes some finite value by adding all of the information relating

to spatial resolution, such as the X-ray CT scanner and image reconstruction. Based on this, the PSF indicates how the spread of an infinitesimally small point in the sample is imaged. Thus, the PSF is mathematically expressed as the imaging of a delta function, as shown below:

$$PSF(x,\ y)R\{\delta(\xi,\eta)\} \tag{7.20}$$

Here, the function $R\ (\xi,\ \eta)$ is the system response and coordinates $(x,\ y)$ and $(\xi,\ \eta)$ are for the detector and sample, respectively. As shown above, the image $g\ (x,\ y)$ is expressed with the following convolution integration [15]:

$$g(x,y)\int\int_{-\infty}^{\infty} f(\xi,\eta)PSF(x-\xi,y-\eta)d\xi d\eta \tag{7.21}$$

Figure 7.21a shows a schematic of the PSF. Furthermore, Fig. 7.22a shows the original image with the point-like structure and the image after this that was imaged [16]. A narrower spreading width of the PSF results in less image blur and a superior spatial resolution.

Imaging point structures, which are smaller than the pixel size, are possible, for example, with medical CT scanners by using a phantom where a 0.1-mm diameter metal wire is floated in the air. However, this is not practical for industrial X-ray CT scanners, particularly those that use a microfocus tube with a small effective pixel size. For example, the QRM GmbH sells test objects that float 3-, 10-, and 25-μm diameter tungsten wires in the air for micro-tomography use [17]. However, this can be used for assessments with a spatial resolution of several dozen μm at most.

The PSF could be expressed in 1D if it were isotropic, as shown in Fig. 7.21. This is referred to as the *line spread function* (*LSF*). Figure 7.21b shows a schematic of the LSF and Fig. 7.22b shows an image for this case as well [16]. As was also the

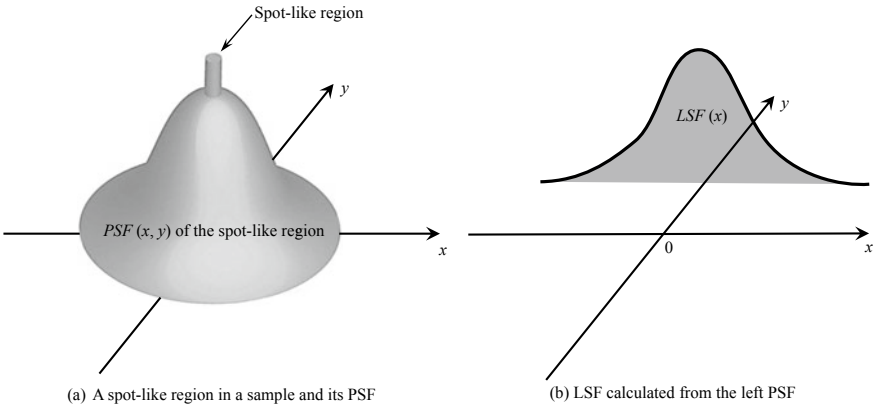

Fig. 7.21 Schematic showing the relationship between the spot-like region in a sample and its PSF and the LSF, which corresponds to its 1D profile. **a** is a spot-like region in a sample and its PSF; and **b** is LSF calculated from the PSF

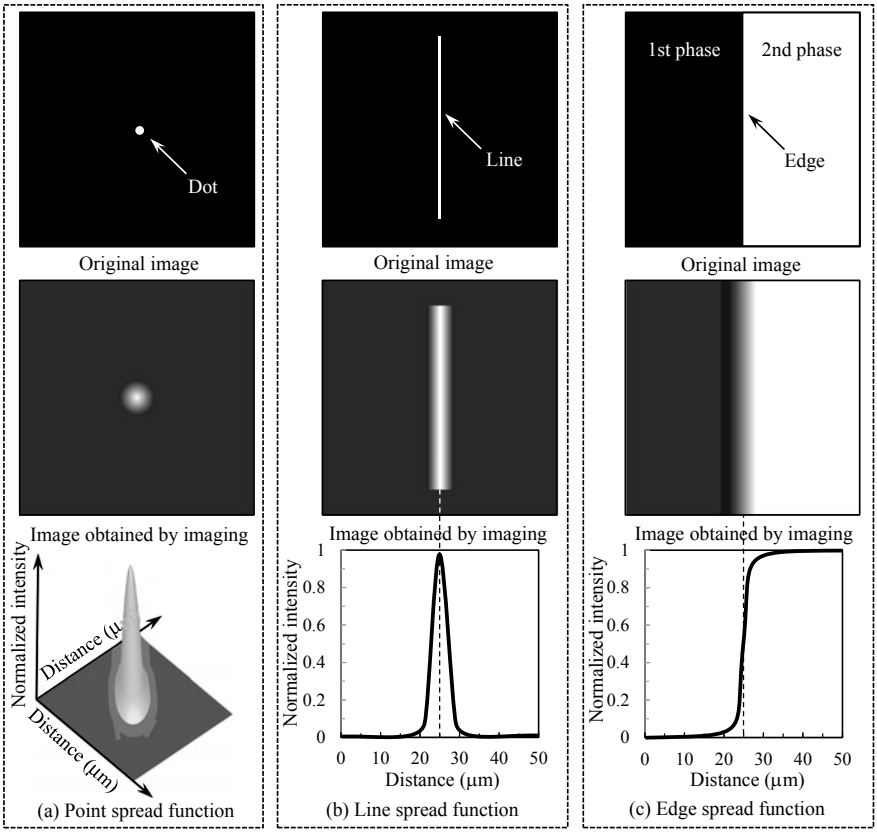

Fig. 7.22 Schematic showing the original image expressed with PSF, LSF, and ESF; the original image blur; and the shapes of each function. **a** is point spread function; **b** is line spread function; and **c** is edge spread function

case in Eq. (7.21), the image can be shown as a 1D convolution of the original image and the LSF [15].

$$g(x) \int_{-\infty}^{\infty} f(\xi) LSF(x - \xi) d\xi \tag{7.22}$$

A slit with a narrow width can be used for LSF measurements. The following relationship is present between PSF and LSF [15].

$$LSF(x) \int_{-\infty}^{\infty} PSF(x, y) dy \tag{7.23}$$

As such, the LSF value at a given position x is equal to the cross-sectional area of PSF in the plane parallel to the y-axis for the same x-coordinates. Furthermore, the relationship between the width of LSF spread and spatial resolution is the same for PSF, which is often two-dimensionally isotropic; the LSF also exhibits bilateral symmetry in this case.

Similarly, the effect where blurring occurs between the interface of the two phases can be assessed using the *edge spread function* (*ESF*). This is shown in Fig. 7.22c [16]. This is mathematically expressed as a step function response where LSF becomes the derivative of ESF [15]:

$$\frac{d}{dx}ESF(x) = LSF(x) \tag{7.24}$$

As shown in Fig. 7.22, the ESF becomes a measure for 1D spatial resolution similar to the LSF. Focusing on practical applications, as some edges are always embedded in the sample, ESF measurements could be termed more versatile than LSF measurements, which require the preparation of a narrow slit.

The PSF, LSF, and ESR are all functions that describe spatial resolution in real space. In terms of practical use, the full widths at half maximum (FWHM) of the PSF and LSF can be used as indices for spatial resolution. Figure 7.23 shows a schematic of this. When the distance between two characteristic points approaches the FWHM, a locally stacked profile comprising the PSF or LSF profiles of the two characteristic points is measured, as shown in Fig. 7.23b. There is still a depression in the center of the curve in Fig. 7.23b, so the two characteristic points can still be distinguished. The two points cannot be distinguished if the distance between these two points is smaller (Fig. 7.23c). As previously mentioned, LSF is determined from the differentiation of ESF, so ESF can also be used for spatial resolution assessments based on FWHM.

(2) MTF

Another standard practice is to convert the PSF, LSF, and ESF discussed in the previous section into the frequency space, assessing spatial resolution with the *modulation transfer function* (*MTF*). An overview of this is provided in this section.

As shown in the following equation, an *optical transfer function* (*OTF*), which is a spatial resolution assessment index in frequency space, can be obtained by applying a 2D Fourier transform on the PSF as shown in Eq. (3.5).

$$OTF(u, v) = F\{PSF(x, y)\} \tag{7.25}$$

Conversely, the PSF is obtained by applying an inverse Fourier transform on the OTF. The OTF is a complex number, and its absolute value is equal to MTF as shown in the following equation. Meanwhile, the phase component of OTF is referred to as the *phase transfer function* (*PTF*).

$$OTF(u, v) = MTF(u, v)e^{-iPTF(u,v)} \tag{7.26}$$

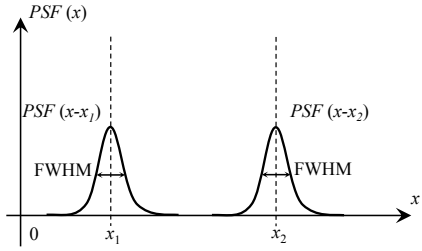

(a) The distance between two points larger than the FWHM of a PSF

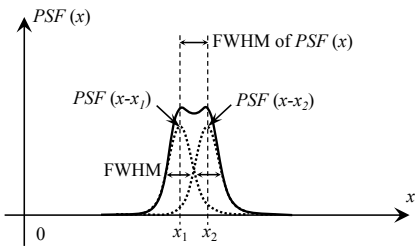

(b) The distance between two points comparable to the FWHM of a PSF

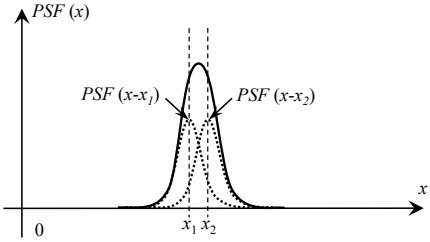

(c) The distance between two points smaller than the FWHM of a PSF

Fig. 7.23 Schematic showing the validity of spatial resolution assessments based on PSF, LSF, and ESF. Three PSF cases are shown where the distance between the two points relative to the FWHM of PSF is significantly larger, equal, or narrower. **a** the distance between two points larger than the FWHM of a PSF; **b** the distance between two points comparable to the FWHM of a PSF; and **c** the distance between two points smaller than the FWHM of a PSF

The PSF generally has an isotropic form, so the phase component PTF becomes 0. The MTF is then related to PSF as shown in the following equation:

$$MTF(u, v) = |OTF(u, v)| = |F\{PSF(x, y)\}| \tag{7.27}$$

In this manner, the MTF is a 2D function. However, considering the general ease of visual assessments, this is frequently assessed as a 1D profile that follows a given axis that passes through the origin of the frequency space. The MTF, in this case, is related to LSF and ESF as shown in the following equation:

$$MTF(u) = F\{LSF(x)\} = F\left\{\frac{d}{dx}ESF(x)\right\} \tag{7.28}$$

MTF assessment is enabled by measuring the LSF and ESF. The MTF generally uses the value at the origin of the frequency space LSF (0) and is expressed by normalizing MTF (u) in the range of 0–1.

Figure 7.24 shows an example of an assessment using the MTF. The horizontal axis of Fig. 7.24 is spatial frequency. Changes in the resolution characteristics can

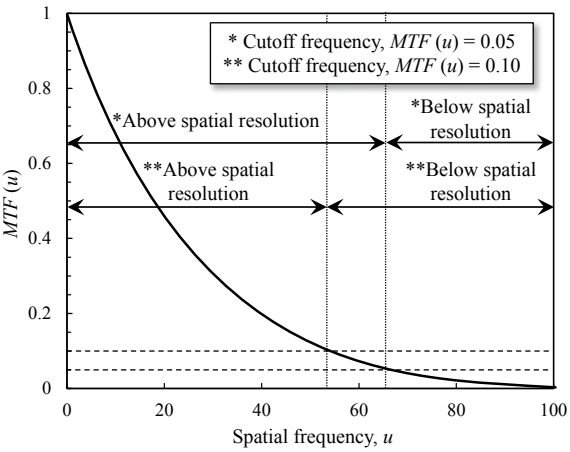

Fig. 7.24 Schematic showing examples of spatial resolution assessments using the MTF. Two analysis examples where the cutoff frequency was changed are shown

be assessed as a function of the spatial frequency using the MTF, which is a function of spatial frequency. In other words, superior resolution characteristics are obtained when these values are closer to $MTF\ (u) = 1$ for a given spatial frequency. As shown in Fig. 7.24, the spatial resolution is often stipulated by the spatial frequency values when the $MTF\ (u)$ value is 0.05, 0.10, or 0.20. These are expressed as 5% MTF, 10% MTF, etc.

The relationship between the ultimate spatial resolution calculated in a 3D image and the various factors that constrain it, which are listed in Table 7.2, was previously discussed in Sect. 7.5.1 (1). Expressing this with MTF yields the following equation [18]:

$$MTF_{total}(u) = MTF_1(u) \cdot MTF_2(u) \cdot \cdots \cdot MTF_k(u) \cdot \cdots \tag{7.29}$$

Here, MTF_{total} is the total MTF, k is the kth factor out of the various factors listed in Table 7.2, and $MTF_k\ (u)$ is the corresponding MTF. However, there is a relationship between MTF and spatial frequency such as that shown in Fig. 7.24 for each factor (e.g. detector, X-ray source). In these cases, $MTF_{\text{total}}\ (u) \leqq MTF_k\ (u)$ is satisfied for all u and v values. Furthermore, the following relationship between the various factors in Table 7.2 and the total FWHM of the LSF is obtained when the spatial resolution is expressed in terms of the FWHM of the LSF [18]:

$$FWHM_{total} = \sqrt{FWHM_1^2 + FWHM_2^2 + \cdots + FWHM_k^2 + \cdots} \tag{7.30}$$

Thus, for an FWHM relating to a factor A, which constrains the final spatial resolution ($FWHM_{\text{A}}$), when the FWHM for a given factor B ($FWHM_{\text{B}}$) is such that $FWHM_{\text{B}}/FWHM_{\text{A}} = 0.1$, the influence of FWHM_{B} on the total FWHM is at most 0.5%. In other words, improvements in spatial resolution require the specification of factors that constrain the spatial resolution and the implementation of countermeasures for improving the spatial resolution with those factors. Equation (5.29) should be referenced in conjunction with this.

7.5.3 Spatial Resolution Measurement

Representative examples of spatial resolution measurement methods are outlined below. There are a number of methods besides these and their variations are numerous. This is not a problem when using the same method to assess 3D images obtained with similar materials/measurement methods, but sufficient care must be taken when comparing spatial resolution values obtained with different spatial resolution measurement methods. For this reason, publications and reports must detail the spatial resolution measurement methods and their associated conditions.

(1) 3D Test Object

A 2D test chart is created by placing a series of parallel line regions on a substrate with considerably different absorption coefficients. This is used for the adjustment of the focal point of the microfocus tubes via transmission images and the maintenance/management of industrial X-ray CT scanners. Spatial resolution measurement test specimens (a.k.a. "3D testing charts") are also commercially available. Figure 7.25a shows a *test object* (corresponding to a phantom in medical terms) for spatial resolution measurement use, produced by the Japan Inspection Instruments Manufacturers' Association (JIMA) [19]. Three grooves are created for each of the vertical and horizontal directions on a silicon chip using micromachining techniques for semi-conductors, gold is embedded in these etched grooves, and the silicon chip itself is embedded into a 2-mm diameter acrylic stick. The line widths and line spacing are 3, 4, 5, 6, and 7 μm. Some 3D test objects are produced in Germany; those with a line width of 1 μm come in two variations: one with 10 spatial resolution levels between 1–10 μm, and one with 9 spatial resolution levels at 5, 10, 15, 20, 25, 30, 50, 100, and 150 μm [20]. As these are simply grooves placed in silicon, the JIMA-produced test objects are widely used internationally.

Figure 7.25b shows a test object used by the author for the 3D imaging of steel. Grooves are placed in a 0.5-mm diameter stainless steel wire with focused ion beam (FIB) fabrication and a spatial resolution measurement across 28 levels with line widths ranging from 0.5 to 5.9 μm can be conducted. Figure 7.26 shows the spatial resolution when the test object in Fig. 7.25b is used to visualize steel materials with synchrotron radiation X-ray tomography [21]. In these cases, spatial resolution is assessed in 3D by measuring it in two directions with the test object, as shown in Fig. 7.25b, and in one direction with the edge spread function shown in Sect. 7.5.2 (1). Decreases in spatial resolution appear due to the forward scattering of X-rays when the camera length is short and, particularly, when high-energy X-rays are present. Furthermore, the spatial resolution in the vertical direction is superior when compared to that in the horizontal direction. This is because the front end slit stipulates that the beam sizes in the horizontal and vertical directions are 400 and 15 μm, respectively; therefore, blurring in the horizontal direction cannot be avoided due to the penumbra [21].

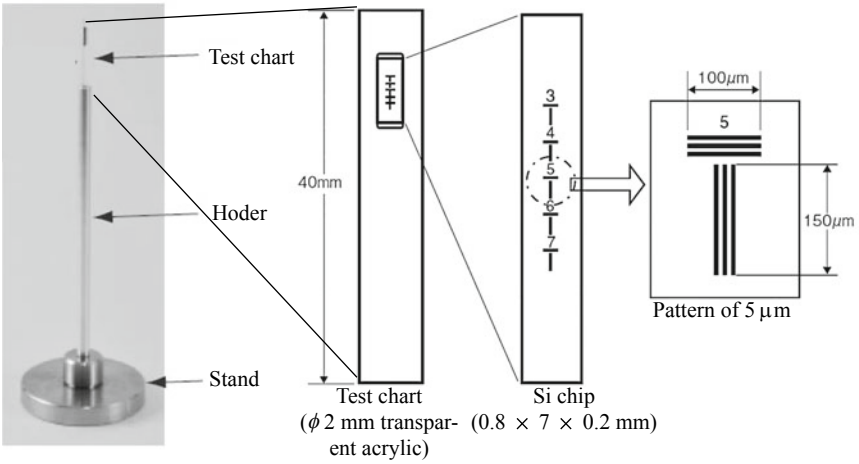

(a) Test chart for X-ray CT provided by JIMA

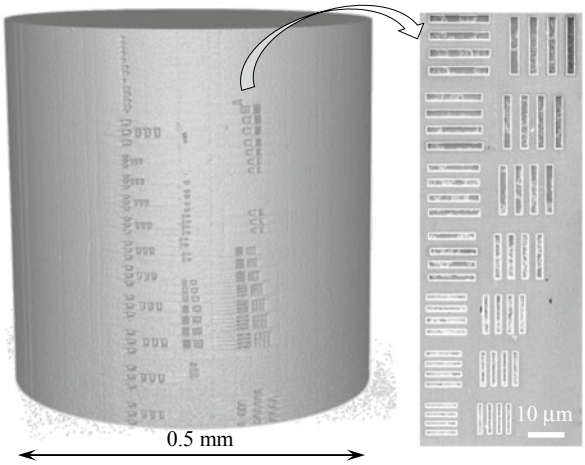

(b) Self-made 3D test chart prepared by the author using FIB

Fig. 7.25 Example of a 3D test object for X-ray CT; **a** is the test object used for spatial resolution measurements produced by the Japanese Inspection Instruments Manufacturers' Association (JIMA) (from the JIMA catalog) with approval from JIMA for publication [19] and **b** is a device made by the author where FIB was used to create grooves on a stainless steel wire surface. The right-hand side shows a magnification of a selected part (3D image from X-ray CT) [21]

The simplest method for measuring spatial resolution while using the test object is to objectively determine the limit at which a contrasted pattern can be identified in a virtual cross-section of a 3D image. However, this can introduce ambiguity due to individual decision standards. For this reason, the spatial resolution is often determined based on the spatial frequency reaching a given MTF value, as discussed

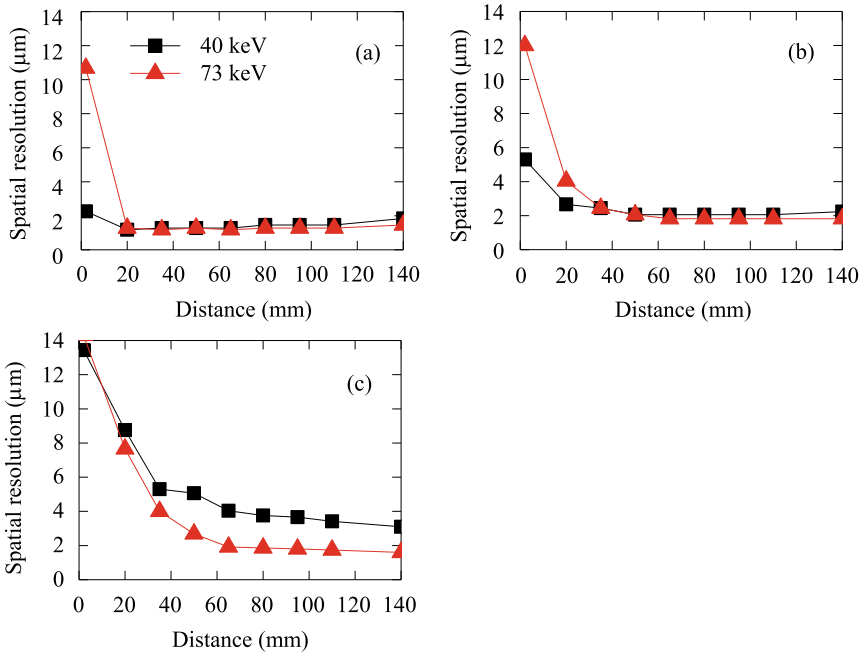

Fig. 7.26 Example where 3D imaging of steel was conducted using X-ray tomography at BL20XU in SPring-8 and where the spatial resolution was measured at two different X-ray energy levels while changing the distance from the sample and detector [21]. The 3D test object of Fig. 7.25 (**b**) was used for the z- and -directions (**a** and **b**, respectively). The edge spread function discussed in Sect. 7.5.2 (1) was used for the r-direction (**c**) in cylindrical coordinates (r, φ, z) corresponding to the rotation axis of the sample rotation stage

in Sect. 7.5.2 (2). This procedure determines the contrast between the groove and space sections of the test object and determines the input/output contrast ratio [18], as shown in the following equation.

$$MTF(u) = \frac{\frac{g_{\max}(x) - g_{\min}(x)}{g_{\max}(x) + g_{\min}(x)}}{\frac{f_{\max}(x) - f_{\min}(x)}{f_{\max}(x) + f_{\min}(x)}} \tag{7.31}$$

Here, $f_{\max}(x)$ and $f_{\min}(x)$ refer to the maximum and minimum values of the primitive function $f(x)$, respectively, whereas $g_{\max}(x)$ and $g_{\min}(x)$ refer to the maximum and minimum values of the image $g(x)$, respectively. Comparisons between two different devices can be conducted with sufficient reproducibility if the test objects are accurately fabricated. Another advantage is that the spatial resolution measurement can be easily verified from an objective standpoint with regards to the obtained image. Meanwhile, only specified spatial frequencies held by the test object can be measured,

so the accuracy of spatial resolution measurements becomes a problem if the device cannot perform in the vicinity of that specified spatial frequency. Furthermore, a single period of the periodic structure of the test object must be accurately identified from the image data and a length that is its integer multiple must be accurately measured [22]. For these reasons, this must be measured by a sampling frequency that satisfies the sampling theorem as shown in Eq. (7.18) [22]. However, it is often the case with spatial frequency near the spatial resolution that there may only be a few pixels' worth of sampling points for each period of the periodic structure of the test object. There have been several reports on methods that increase the measurement accuracy in these cases. Please refer to these as required [22].

(2) Edge Response

Methods discussed in Sect. 7.5.2 (1) for analyzing the edge spread function have the advantage of directly measuring spatial resolution from 3D images of samples to be observed without using specialized devices. These methods are widely used and measure the edge sections of sample surfaces or sample interiors: in other words, the pixel transitions (i.e., edge responses) in the boundary sections, such as between the sample and air. After determining the ESF in this manner, the ESF is differentiated to calculate the LSF, and either its FWHM is determined or a Fourier transform is applied on the LSF to determine the MTF. This MTF-based method is recommended in ASTM E1570-11. The ESF is determined by approximating the pixel value transitions in the obtained image with a sigmoid function as shown in the following equation:

$$ESF(x) = \frac{a}{1 + e^{(-bx+c)}} + f \tag{7.32}$$

Here, a, b, c, and f are coefficients that determine the translation, amplification, and width of the transition zone in the S curve. Figure 7.27 shows a schematic of the ESF where three different spatial resolution levels were obtained by varying the coefficients in the sigmoid function. The differences in spatial resolution expressed as the width of the transition zone can be clearly expressed by the differences in the coefficients of Eq. (7.32). Previous reports, which measured the spatial resolution by using the edge response, have used polynomial approximations, error functions, [23] or the sum of Gaussian functions and exponential functions [24]. The accuracy of the approximations directly influences MTF measurement accuracy, therefore, an optimal function must be selected.

Pixel value transitions, which span the edge, must be measured at a sampling frequency that satisfies the sampling theorem in Eq. (7.18) similar to the test object case when assessing the edge response. However, it is often the case that there is only a few pixels' worth of sampling points (pixels) in the pixel value transition zone across the edge when using high-spatial-resolution devices whose spatial resolutions are stipulated by the sampling pitch based on the sampling theorem. There have been reports of accuracy increases in these cases. A representative example is the inclined edge method. This method is also standardized by ISO12233 [25]. The

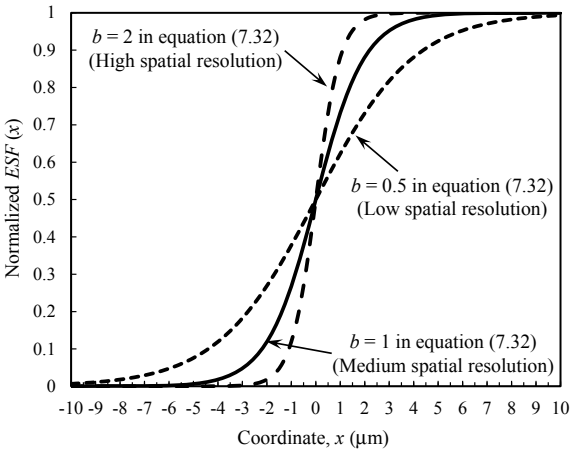

Fig. 7.27 Sigmoid function types. From Eq. (7.32), $a = 1$ and $c = f = 0$, and a normalized ESF was displayed by varying b to reflect high, medium, and low spatial resolutions

inclined edge method measures an edge response on straight edges or two-phase boundaries/surfaces that are inclined only slightly from the pixels of the 2D detector by approximately 1.5–3°. The alignment is slightly shifted for each pixel along the boundary due to this inclination. This is shown schematically in Fig. 7.28. Integrating the data in the direction along the boundary at a sampling pitch considerably smaller than the pixel size of the 3D image along the boundary allows for a high-density measurement of the pixel value profile across the edge and the determination of a synthesized LSF. As mentioned previously, the ESF is often approximated by fitting it to a function whose shape is similar to the edge response. Meanwhile, with ISO12233, space is divided by 1/4 of the pixel size, and discrete data are obtained by averaging the values inside these subpixels.

A smooth surface or interface in the sample interior, which is sufficiently below the spatial resolution, must be used to apply the inclined edge method. If this is not the case, then a test object must be prepared to conduct spatial resolution measurements of physical objects that have a similar smooth edge.

Figure 7.29 shows a 3D image of a high-purity aluminum alloy obtained using SPring-8. The sample-detector distance in Fig. 7.29b was intentionally set as long and the interface between the sample and air (sample surface) was highlighted by the black-and-white fringes created using the refraction contrast imaging. The voxel size of the 3D image in this was 0.5 μm and the effective spatial resolution was approximately 1 μm. Figure 7.30 shows the ESF obtained using Eq. (7.32) to approximate the pixel value transitions at the interface of the image shown in Fig. 7.29; this was then differentiated to calculate the LSF. The center of the figure also shows the LSF calculated by directly differentiating the measured ESF data. The LSF directly determined from the ESF is not bilaterally symmetric. This was primarily thought to be due to the X-ray refraction between the aluminum-air interface. Additionally,

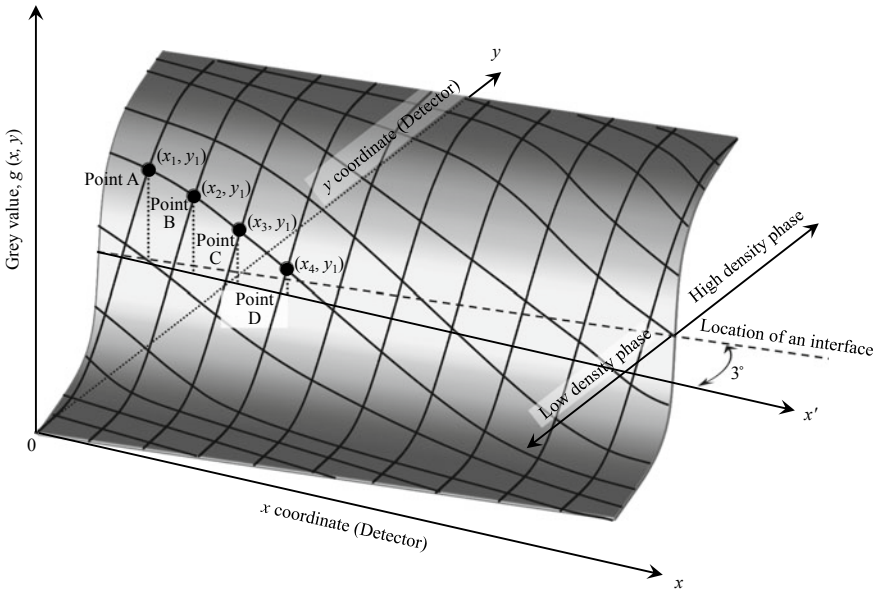

Fig. 7.28 Schematic showing the 2D measurement of pixel values along an interface, which has a slight inclination relative to the high-density and low-density phase edge orientation in terms of the coordinates of the detector. Points A–D in the figure are measurement points, which lie on the x-axis of the same y-coordinate (y_1) ($x_1 < x_2 < x_3 < x_4$). The pixel value gradually decreases from Point A to Point D as this becomes further and further away from the interface; i.e. the edge of the high-density phase, which has a large pixel value with a pitch that is considerably lower than the pixel size

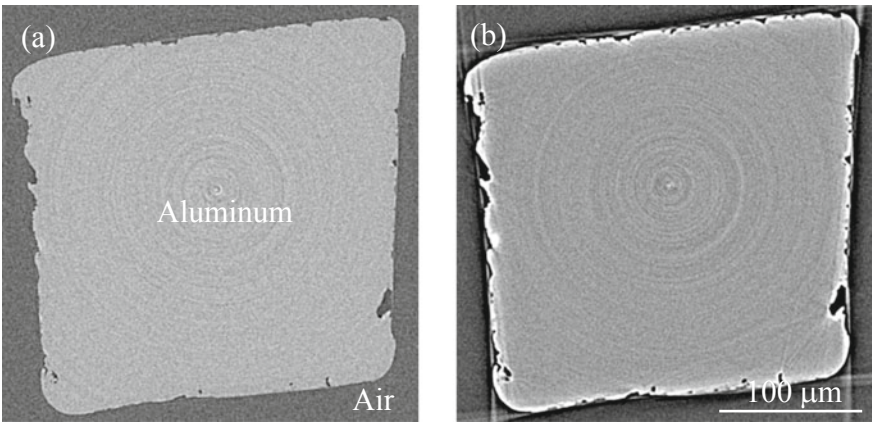

Fig. 7.29 Cross-section image (raw data) of pure aluminum (99.999%) imaged with synchrotron radiation X-ray tomography at the BL20XU beamline in SPring-8. Images were taken with an X-ray energy of 20 keV and reconstruction was based on filtered back projection using the Hann filter; **a** is when the sample-detector distance is 3 mm and **b** is when the distance is 55 mm (courtesy of Kazuyuki Shimizu of Kyushu University)

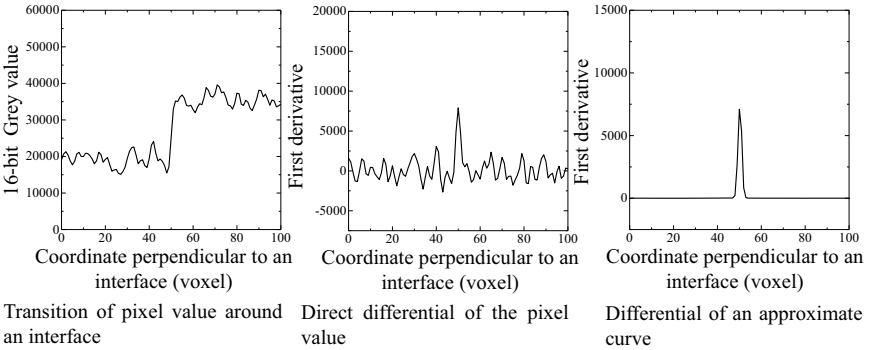

(a) Sample-to-detector distance of 3 mm

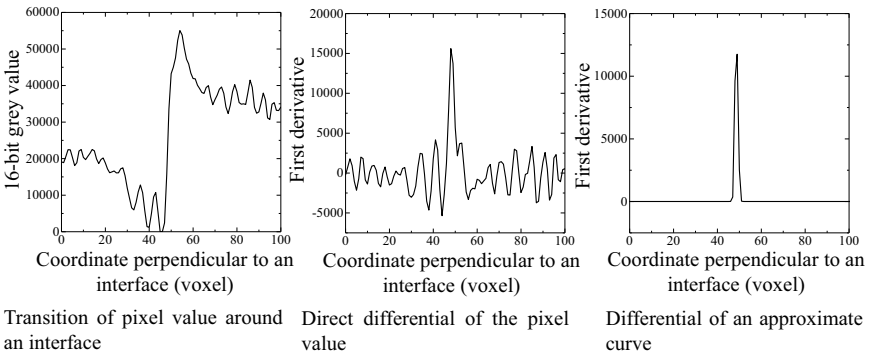

(b) Sample-to-detector distance of 55 mm

Fig. 7.30 Pixel value transitions were measured in the aluminum-air interface of the 3D images in Fig. 7.29 (left), which were either directly differentiated to obtain the LSF (middle) or the pixel value transitions at the interface were fitted with a sigmoid function, which was then differentiated (right). **a** sample-to-detector distance of 3 mm; and **b** sample-to-detector distance of 55 mm. (courtesy of Kazuyuki Shimizu of Kyushu University)

a similarly asymmetric LSF is generated with beam hardening, which is a representative artifact present in industrial X-ray CT scanners. The asymmetry of LSF is more prominent when the sample-detector distance in Fig. 7.30 is long. Consequently, sufficient care must be taken when measuring different spatial resolution values between the interfaces between dissimilar phases in the sample interior and sample surface, in cases where refraction or artifacts at the matrix–air interface of the sample surface are prominent.

Figure 7.31 shows the MTFs obtained by applying a Fourier transform on the LSF calculated by directly differentiating the ESF and on the LSF obtained by differentiating an approximation curve for the ESF. Figure 7.30 shows an undershoot (i.e., the skirts of the peak have negative peaks on both sides) for the LSF. This results in an overshoot of the MTF in values above 1 in Fig. 7.31. The LSF undershoot is due to the enhancement of the edges; the usage of filter functions during reconstructions, which can produce artifacts near the edges; X-ray refraction at the interface; and

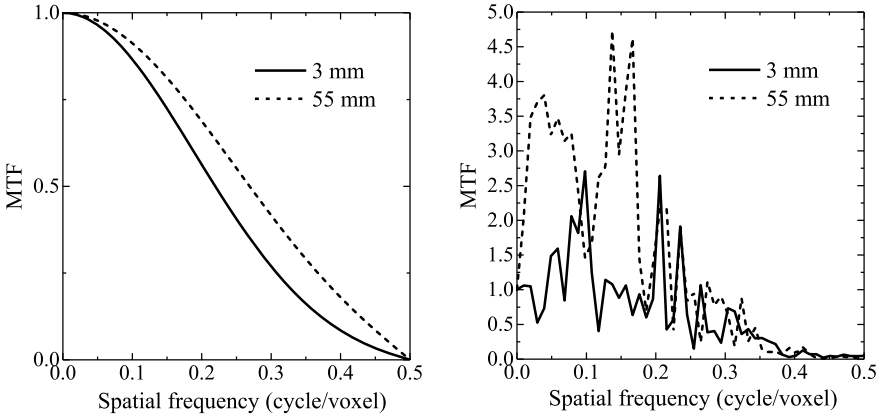

(a) MTF obtained from ESF of the curve approximated with a sigmoid function

(b) MTF obtained from directly measured ESF

Fig. 7.31 MTF obtained by applying a Fourier transform on the LSF in Fig. 7.30. Comparison between the MTF obtained from the LSF after fitting the pixel value transitions in the interface with a sigmoid function and differentiating it in **a**, and the MTF obtained from the LSF after directly differentiating the pixel value transitions in the interface in **b**. (courtesy of Kazuyuki Shimizu of Kyushu University)

beam hardening artifact generation. Furthermore, the fluctuations in the skirts of the LSF appear as sharp peaks in the MTF curve. Furthermore, the skirt range is smooth when fitted with a sigmoid function, so no fluctuations in the curve are observed.

Comparisons of the spatial resolutions determined in this way are shown in Table 7.3. When using the FWHM of the LSF to measure the spatial resolution, a likely spatial resolution is obtained for cases where an approximative curve was obtained with a sigmoid function. Measurements with the MTF yield virtually the same values independent of the large curve fluctuations in the low spatial frequency domains shown in Fig. 7.31, regardless of whether an approximative curve was used,

Table 7.3 Spatial resolutions measured using the data from Fig. 7.30 obtained from the image in Fig. 7.29; Comparisons of spatial resolutions determined from the LSF FWHM for the two sample-detector distance levels and the spatial resolutions stipulated by the spatial frequency value when the *MTF* (*u*) value was 0.05, 0.10, or 0.20 (courtesy of Kazuyuki Shimizu of Kyushu University) (μm)

ESF measurement method	Sample-to detector distance	FWHM	MTF		
			5% MTF	10% MTF	20% MTF
Fitting with a sigmoid function	3 mm	1.1	1.2	1.3	1.5
	55 mm	1.0	1.1	1.1	1.3
Measured value	3 mm	1.2	1.2	1.3	1.3
	55 mm	1.4	1.2	1.3	1.4

or the measured data was used directly. The 5% MTF value is close to the FWHM-based measured values in this case and a probable spatial resolution can be obtained. In either case, there is an error of approximately 50% according to measurement methods, therefore, it is important to compare the spatial resolutions with the same measurement method/measurement conditions.

7.6 Artifacts

This section provides a comprehensive introduction of *artifacts*, which are unavoidable in X-ray tomography, encountered often in industrial X-ray CT scanners and synchrotron radiation X-ray tomography. Here, the industrial X-ray CT scanner for micro-tomography (Skyscan 1072: X-ray tube voltage of 20–100 kV, spot size of <5 μm, 14-bit cooled CCD detector), which can be freely used by the author, was used to for imaging and reconstruction under conditions that intentionally generated artifacts, as shown in the corresponding figures. Artifacts encountered during experiments at SPring-8 are also included here. These aspects should be kept in mind as unavoidable artifacts are handled during X-ray tomography.

7.6.1 Artifacts Due to Interactions Between X-Rays and Objects

(1) Beam Hardening

Figure 7.32 shows an image of aluminum with a thickness of several mm scanned at a tube voltage of 80 kV using the industrial X-ray CT scanner. Figure 7.32a is an image taken without filtering. The voxel value is large in the vicinity of the sample surface, particularly in the corners, where the X-ray path becomes longer. The aluminum structure is completely homogeneous in the cross-section and the changes in color are due to artifacts referred to as beam hardening, which occur when the X-ray is not monochromatic. According to Fig. 7.10, beam hardening is significant when the exposure time is decreased from a suitable value (380 ms).

The generated X-ray energy when using an X-ray tube has a distribution like those seen in Figs. 4.18 and 4.55. X-ray energies can be distributed across a wide range—up to 80 keV, in the case of the X-ray CT scanner used. Furthermore, as shown in Fig. 2.4 and Figs. 2.10, 2.11, 2.12, 2.13 and 2.14, the linear absorption coefficient has a strong X-ray energy dependency. X-rays with low X-ray energy are absorbed immediately below the surface; only those with relatively high energy transmit to the material interior, resulting in changes to the spectrum of the transmission X-ray.

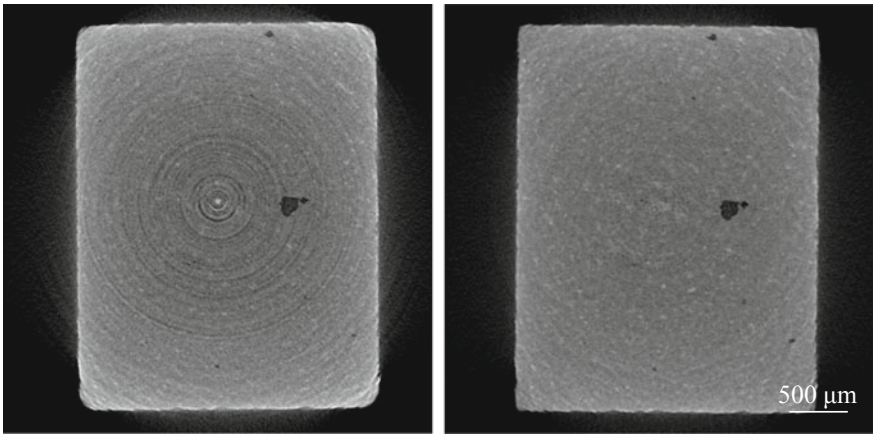

(a) Without a filter (b) With a filter

Fig. 7.32 Cross-section images of aluminum specimens scanned with a Skyscan 1072 and subsequently reconstructed in **a**. The number of projections was 1800 images/180°, the exposure time was 380 ms, and the voxel size was 4.6 μm. A 0.5-mm thick aluminum filter was used in **b**

Equation (2.5) shows the transmission X-ray intensity when the incident X-ray intensity and linear absorption coefficients are expressed as a function of X-ray energy. The projection data p, in this case, are as follows:

$$p = log\left(\frac{I}{I_0}\right) = -log\left(\int_E I_0(E)e^{-\int_0^L \mu(z,E)dz}dE\right) \tag{7.33}$$

In this manner, projections show a nonlinear relationship to transmission length when the X-ray is not monochromatic.

Beam hardening can be prevented by correcting the projection data with theoretically or experimentally derived correction curves [26] or by placing a filter between the sample and X-ray source. Figure 7.32b shows imaging with a 0.5-mm thick aluminum filter. The placement of the filter shows a considerable reduction in beam hardening. In some devices, the filter is automatically selected, like those in Fig. 4.53. The reduction in flux and worsening S/N ratio must also be considered when a filter is applied.

Even when an X-ray tube is used, a suitable combination of the target material of the X-ray tube and filter material can prevent beam hardening by obtaining quasi-monochromatic light. For example, Jenneson et al. obtained quasi-monochromatic light near the Kα X-ray of molybdenum (17.4 keV) by combining with a molybdenum target, a tube voltage of 50 kV, and a 100-μm thick molybdenum filter [27].

(2) X-Ray Scattering Effects

As shown in Fig. 2.10 through 2.13, the Compton effect is predominant at high X-ray energies, where forward scattering tendencies increase. This has an adverse effect on image quality during X-ray imaging. As detailed in Sect. 6.1, this is also the reason why line sensor cameras can achieve a higher image quality than flat panel detectors in industrial X-ray CT scanners when X-ray tube voltages are high.

As previously shown in Fig. 7.26, the spatial resolution decreases significantly, when the sample-detector distance is small and the X-ray energy is high. Figure 7.33a shows a 3D image in this case. The S/N ratio significantly decreased due to the effects of forward scattering. This not only reduces spatial resolution but also affects linear absorption coefficient measurements. In the author's experience, this effect is prominent when the X-ray energy is over 40 keV when imaging steels with monochromatic X-ray. This can be avoided by setting an appropriate distance between the sample

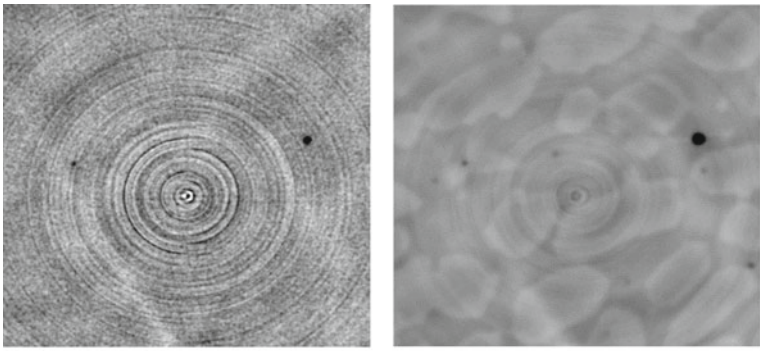

(a) $L = 0.008$ m (b) $L = 0.3$ m

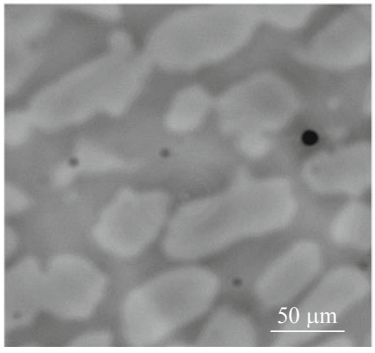

(c) $L = 0.8$ m

Fig. 7.33 Example where 3D imaging of steel was conducted using X-ray tomography at BL20XU in SPring-8 and where the sample-detector distance L varied during measurement [21]. **a**, **b** and **c** are 0.008, 0.3 and 0.8 m in L, respectively. The sample was a two-phase stainless steel and the X-ray energy used was 37.7 keV

and detector, as shown in Fig. 7.33b, c. However, care must be taken as excessive distances can result in gradually decreasing spatial resolution as shown in Fig. 7.26.

(3) X-Ray Refraction Effects

Section 2.2.2 (2) introduced refraction contrast imaging as an imaging method that utilized the geometric optics phenomenon of X-ray refraction. Refraction phenomena not only have positive effects such as emphasizing the contours of the interface or surface but also the negative effect of generating artifacts. These artifacts are particularly evident during synchrotron radiation X-ray tomography.

Figure 7.34 shows representative examples of this. Figure 7.34a shows artifacts that occur in the vicinity and in front of a crack when the X-ray beam is parallel to the crack surface. The aluminum matrix in the vicinity of the crack varies widely in voxel values and it is difficult to accurately segment the crack and specify the coordinates of the crack tip position. Furthermore, the contours of the crack surface are excessively emphasized due to refraction contrast, as shown in section A. This is a major barrier in studying the fatigue crack closure phenomenon. Similar artifacts can be observed in Fig. 8.25a.

Meanwhile, Fig. 7.34b shows artifacts that occur due to the refraction of X-rays from a flat sample side. The right figure shows white lines that do not exist in reality on the extended lines of the surface. These artifacts are not visible in the left figure, where the sample was placed immediately adjacent to the detector. Fringes that were effectively used for emphasizing contours in refraction contrast imaging are excessively generated in the right figure, where the sample-detector distance is longer. In these cases, the fringes conversely act to inhibit the accurate determination of the sample surface position/shape.

(4) Metal Artifacts

Figure 7.35 shows a cross-section with excessive gallium present on an aluminum surface following a liquid gallium coating applied in the liquid metal wetting technique (discussed in Sect. 5.5.1). As shown in Fig. 2.4, the linear absorption coefficients of gallium and aluminum vary by a factor of several dozen at X-ray energies of over 10 keV. Streaks extend radiatively in the vicinity of the highly-X-ray-absorbing gallium with it at the center. These are also referred to as streak artifacts. However, many other elements cause streaks, so the term *metal artifact*, which occurs with human body/metal implant combinations in medical X-ray CT scanners, is used here.

The mechanism by which metal artifacts occur is not straightforward. In other words, various factors such as artifacts due to beam hardening or photon depletion, scattering, refraction effects, detector characteristics, etc. overlap with the presence of high X-ray absorption phases.

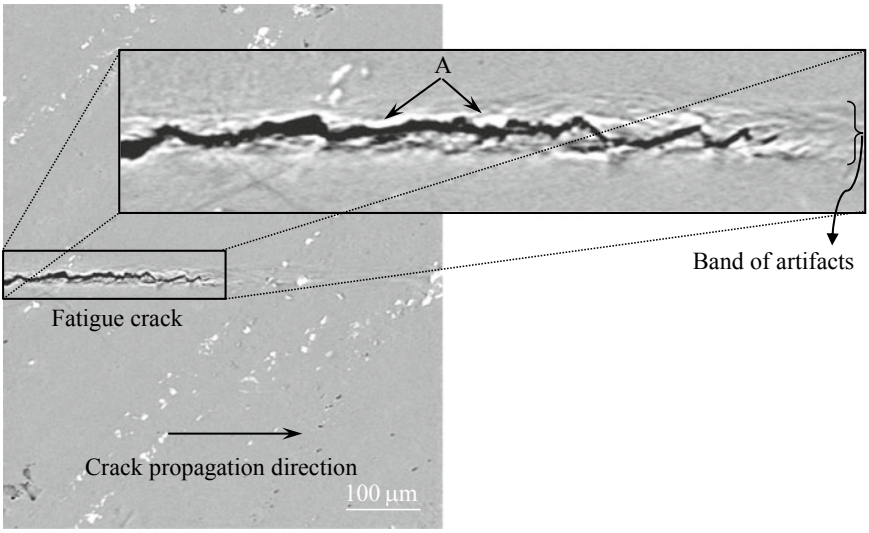

(a) Artifacts observed in the vicinity of a crack propagating in parallel to an X-ray beam

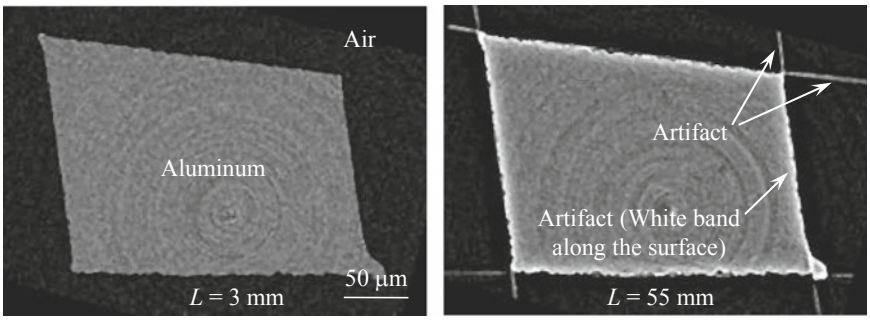

(b) Artifacts stemming from flat sample surface

Fig. 7.34 Examples of artifacts due to X-ray refraction; **a** is the vicinity of a fatigue crack tip in A7075 aluminum alloy and its magnification and **b** is an Al–Cu alloy. Experiments were conducted at BL20XU in SPring-8 and the sample-detector distance was set as 55 mm, except for the left figure in **b**. The X-ray energies were all 20 keV (courtesy of Shohei Yamamoto, who was a graduate of the author's laboratory (currently at NTN Co.); and Kazuyuki Shimizu of Kyushu University)

7.6.2 Artifacts Due to Device

(1) Ring Artifacts

Ring-like artifacts were observed in the cross-section images of Figs. 5.23, 7.10, 7.16, 7.32, 7.33, etc., in the x–y plane, where the orthogonal coordinate system was set such that the z-direction was parallel to the sample rotation axis. These are referred to as *ring artifacts*. The center of the ring artifact is the center of rotation. These are popular artifacts in X-ray tomography and occur due to nonlinear responses of

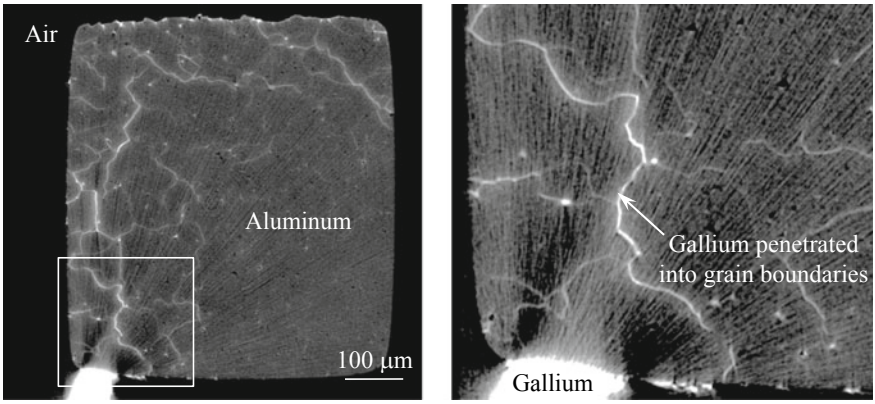

(a) Whole image

(b) Magnified view of the region highlighted with a white rectangle in (a)

Fig. 7.35 Example of metal artifacts. The high X-ray absorbing gallium was affixed to the surface of the aluminum alloy and artifacts were produced near the vicinity of the gallium. Experiments were conducted at BL20XU in SPring-8, the sample-detector distance was 55 mm, and the X-ray energy was set at 20 keV. **a** the whole cross section; and **b** a magnified view of the region highlighted with a white rectangle in **a**

part of the pixels in a detector. These appear even more emphatically when there is electrical/thermal instability in the detector, variation in the X-ray beam, and insufficient exposure time. If the ring artifact occurs near the center of rotation, the sample or the important observation regions in the sample should be offset in the field-of-view if possible.

The standard filtering processes discussed in Sect. 8.1 are not suitable for the removal of ring artifacts. There have been numerous reports since the 2000s on filters designed to remove ring artifacts and these should be used instead. ImageJ also allows for ring artifact removal filters through its Xlib plug-in [28].

(2) Artifacts Due to Misalignment

Figure 7.36 shows misalignment between the rotation axis of the sample rotation stage and the detector axis. For example, insufficient adjustment of the tilt angle in detectors may result in the inclination between the axes of the sample rotation stage and the detector during synchrotron radiation experiments. Furthermore, insufficient stiffness of the sample rotation stage and its vicinity may cause inclinations as it sinks even if the sample weight is below the load capacity of the sample rotation stage. Figure 7.37 shows an image where misalignment occurred. A relatively large misalignment of 9 pixels (0.258°) was present in the top edge of the detector surface between the rotation and detector axes. In these cases, even the form of the sample

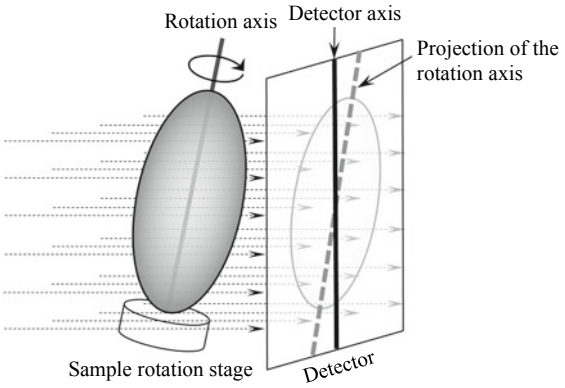

Fig. 7.36 Explanatory figure of when the detector and sample rotation stage axis are misaligned

surface and internal structure could not be accurately measured. Furthermore, the image quality greatly decreased. Quantitative image analysis is difficult in these conditions. If the axis inclination were in the direction shown in Fig. 7.36, this can be corrected at the transmission image stage by rotating the image by an amount equal to the inclination. Corrections are difficult if the inclination is in a parallel direction to the X-ray beam.

(3) Sample Rotation Stage Eccentricity Effects

The positional accuracy of the sample rotation stage (discussed in Sect. 4.3.1) is an important factor that can lead to worsened image quality. Clear artifacts are not generated, creating a further hindrance. An analysis of sample rotation stage eccentricity conducted by the author in the early stages of imaging tomography is introduced in Fig. 7.38 [29]. First, a portion of an aluminum microstructure due to imaging tomography taken with an effective pixel size of 88 nm is shown in Fig. 7.38a. Fine particles with a high X-ray absorption are affixed on the specimen surface and the eccentricity of the sample rotation stage is measured by calculating its trajectory. The eccentricity based on this when the sample was rotated 180° was a maximum of 0.4 pixels with an average of 0.15 pixels. This extent of eccentricity does not influence spatial resolution. The particle image, in this case, is shown in Fig. 7.38a. As shown on the right side of the figures, Fig. 7.38b, c show cases where the eccentricity of the rotation stage was gradual (periodicity of 22.5°) or choppy (periodicity of 0.6°). The transmission images were rotated/translated based on the eccentric trajectory and the reconstructed images obtained for each case were calculated. The eccentricity in each case was ±3 pixels. As can be observed from the figure, the high-frequency case was minimally affected even with the same eccentricity and the particle morphology varied considerably when the eccentric motion was gradual.

(4) Sample Drift

Artifacts can occur during scanning when the sample itself experiences time-dependent deformation or changes. Oftentimes, however, it is due to the sample

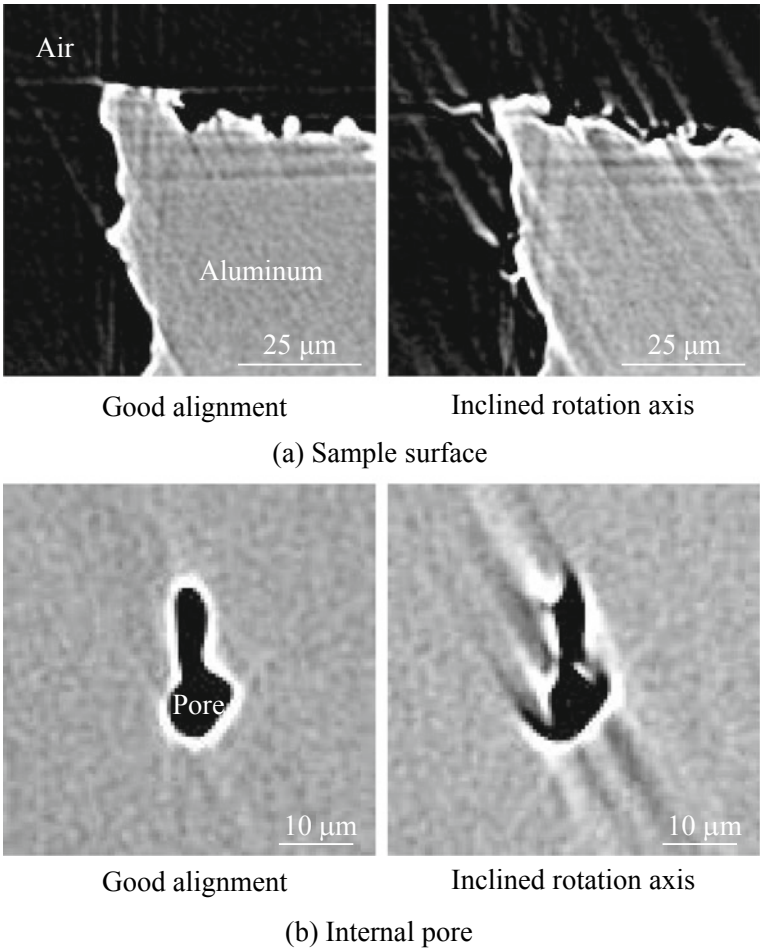

Fig. 7.37 Artifacts when the detector and sample rotation stage axis are misaligned. The detector axis is misaligned by 0.258° (9 pixel) in this case. The sample is an aluminum alloy. **a** sample surface; and **b** an internal pore. Experiments were conducted at BL20XU in SPring-8, the sample-detector distance was 25 mm, and the X-ray energy was 20 keV

being insufficiently fixed. Figure 7.39 shows samples that were intentionally moved vertically or horizontally (i.e., within the detector plane). Examining the directions in which the sample drifted using cross-section images reveals a significant elongation of the pore morphology. Consequently, pores are difficult to confirm on the right-hand side of Fig. 7.39a. Pores can be somewhat identified in cross-section layers that were

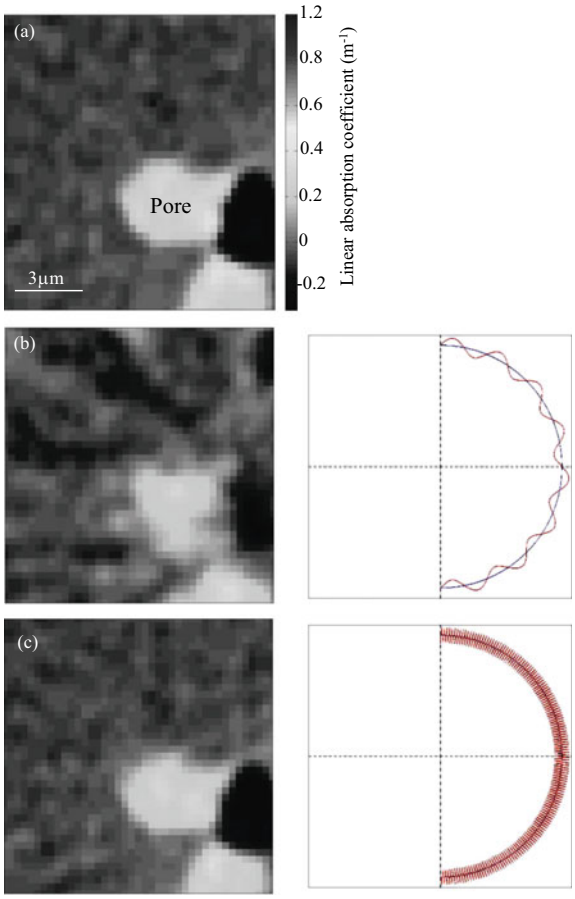

Fig. 7.38 Simulation of the effects of sample rotation stage eccentricity on the reconstructed image [29]. The sample is an aluminum alloy and the figure in **a** shows a magnified image of a particle inside that alloy. Experiments were conducted at BL47XU in SPring-8, the sample-detector distance was 25 mm, and the X-ray energy was 20 keV. The eccentricity patterns are shown in the right-hand sides of **b** and **c**

orthogonal to the sample drift direction like those on the right-hand side of Fig. 7.39b, regardless of whether the sample drift was significant. Comparisons of the 0° and 180° images in the manner described in Sect. 7.2 should be conducted if sample drift is suspected in images. Observations with high spatial resolution require sample fixing methods and sample drift countermeasures that correspond to that spatial resolution. Sufficient consideration must be given to thermal and mechanical stability (creep deformation, stress-relaxation phenomena, etc.) of the sample, particularly with the imaging-type tomography. Furthermore, the reduction of imaging time using fast tomography can be effective in these cases as well.

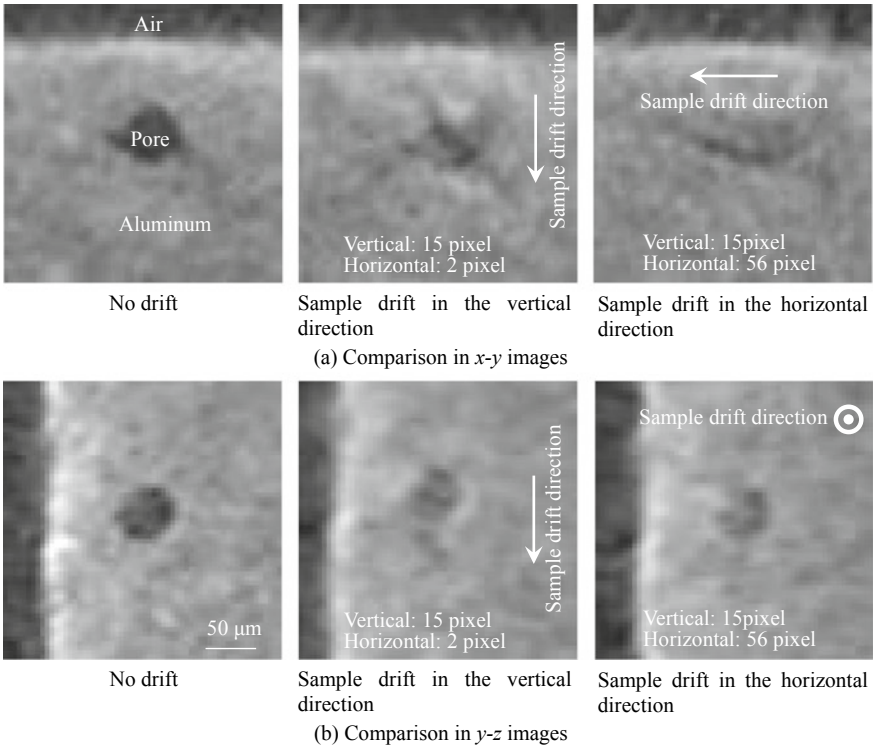

Fig. 7.39 Influence of sample movement on image quality. Reconstructed cross-section images of aluminum specimens scanned with a Skyscan 1072. The exposure time was 380 ms and the voxel size was 4.6 μm. **a** comparison in *x*-*y* plae; and **b** comparison in *y*-*z* plane. The specimen was fixed with scotch tape and left to drift with its own weight in either the vertical (*z*) or horizontal (*x*) directions. The movement amounts written in the figures are the total movement when imaged from 0 to 180°

(5) Cone Beam Artifacts

As discussed in Sect. 3.3.4, cone beam-based imaging exhibits shadows for which data are unobtainable with further distance from the origin in the *z*-axis direction. The image reconstruction accuracy decreases due to this missing data. This influence is more pronounced in industrial X-ray CT scanners as the cone angle increases (i.e. larger magnification) and as the cross-sections are vertically distanced from the center.

7.6.3 *Artifacts Due to Imaging Conditions*

(1) Exposure Time, Projection Number, and Missing Wedge Influences

Similar to Fig. 7.32, Figs. 7.40 and 7.41 show aluminum alloys imaged using industrial X-ray CT scanners, where both the exposure time and projection number were changed to an extreme. The magnification is considerable in these images and the appropriate values for both are an exposure time of 380 ms and a projection number of approximately 1800 projections based on the sampling theorem. Although not in the form of artifacts, large effects are observed in the image quality of both images. Decreasing projection number and exposure time result in large decreases in S/N ratio, spatial resolution, and contrast. The internal structure morphologies in these cases also change when they drop below half of the optimal values. Although not observed in the experiments of Fig. 7.41, artifacts referred to as *aliasing artifacts* occur when the projection number is decreased. All cross-sections of the sample or under-sampled regions show a sequence of streaks that expand outward starting from regions with high absorption coefficients. These can be resolved by simply

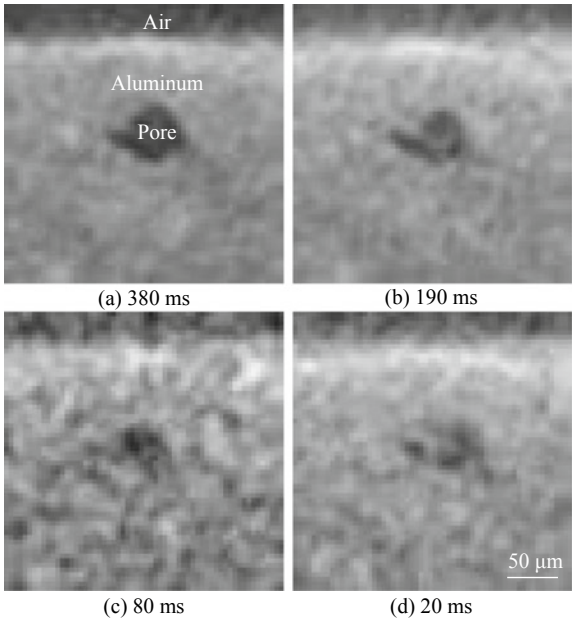

Fig. 7.40 Influence of exposure time on image quality. Reconstructed cross section images where aluminum specimens were scanned with a Skyscan 1072. The number of projections was 1800 images/180^{o} and the voxel size was 4.6 μm. Exposure time is 380, 190, 80 and 20 ms in **a**, **b**, **c** and **d**, respectively

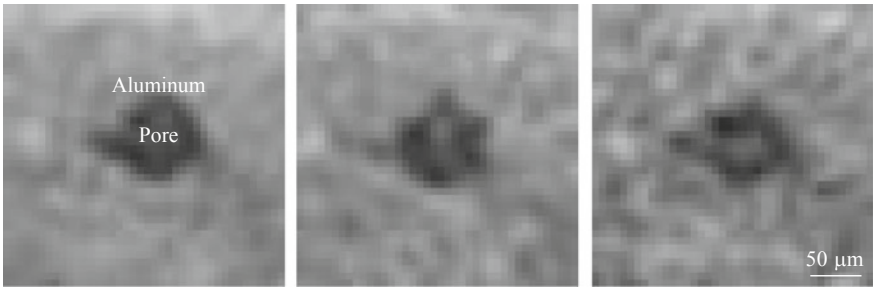

(a) 1800 projections (b) 900 projections (c) 360 projections

Fig. 7.41 Influence of the number of projections on image quality. Reconstructed cross section images where aluminum specimens were scanned with a Skyscan 1072; The exposure time was 380 ms and voxel size 4.6 μm. The number of projections is 1800, 900 and 360 in **a**, **b** and **c**, respectively

increasing the number of projections to the optimal value; these artifacts are not a major problem with standard X-ray tomography.

Next, Fig. 7.42 shows a reconstructed image where a certain range of projections could not be obtained with a 180° rotation angle (the "missing wedge" defect). This corresponds to when the sample size is extremely large in a given direction or when devices for *in situ* observations create a shadow over a certain portion. The data in

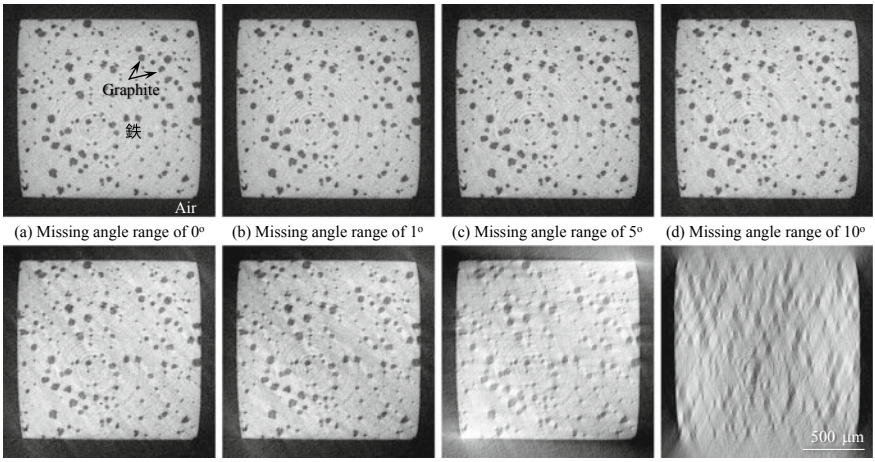

(a) Missing angle range of 0° (b) Missing angle range of 1° (c) Missing angle range of 5° (d) Missing angle range of 10°

(e) Missing angle range of 20° (f) Missing angle range of 30° (g) Missing angle range of 60° (h) Missing angle range of 120°

Fig. 7.42 Influence of missing angle on image quality. Sample is a spherical graphite cast iron. Experiments were conducted at BL20XU in SPring-8; the sample-detector distance was 120 mm, X-ray energy 37.7 keV, and voxel size 1.4 μm. Missing angle range is 0, 1, 5, 10, 20, 30, 60 and 120 in **a**, **b**, **c**, **d**, **e**, **f**, **g** and **h**, respectively

Fig. 7.42 are reconstructed by substituting the data from 1 to 120° with I_0 images. Structural observations can be conducted visually when the missing angle is 30° or less. Microstructure shapes like that of graphite do not change considerably if below 10°. However, further inspection shows a decrease in image quality even with slight angle defects. These effects are evident when the microstructure is barely at the spatial resolution or when observing structures with weak contrast.

(2) X-Ray Beam Diameter Influences

The image reconstruction method of a region of interest from incomplete projection data obtained by irradiating a narrow X-ray on a sample with a large diameter was explained in the discussion of specialized image reconstruction methods in Sect. 3.3.5. Artifacts appear when standard reconstruction methods are applied to samples with a large diameter that unintentionally protrude out of the field-of-view. Figure 7.43 is an example of this. A white fringe can be seen on the edges of the field-of-view. If these have large effects on image assessment, measures such as the application of a specialized reconstruction method, expansion of the field-of-view, or reduction in sample size are necessary. However, the locations at which the artifacts appear are limited, hence, frequently; this may not have adverse effects on assessment.

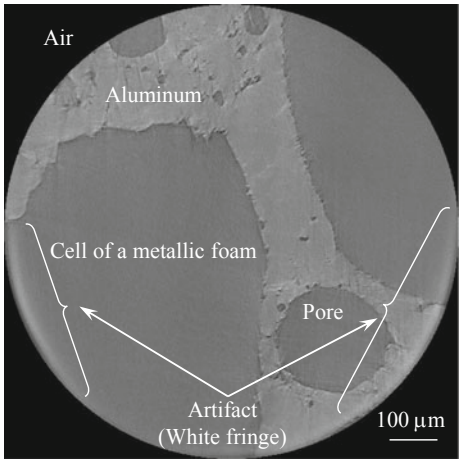

Fig. 7.43 Artifacts appearing in an image reconstructed with standard reconstruction methods when a specimen that is considerably larger than the field of view size is used. The sample was a porous aluminum alloy with a diameter of 7 mm, using a beam width of 1 mm. Experiments were conducted at BL47XU in SPring-8, the sample-detector distance was 55 mm, and the X-ray energy was 20 keV

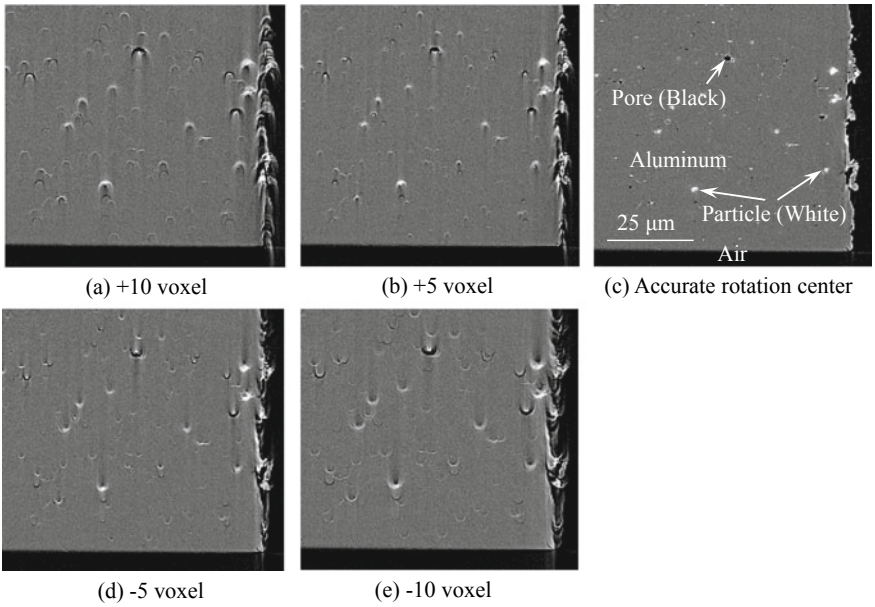

Fig. 7.44 Artifacts due to misalignment of the reconstruction center. Reconstructed cross section image where an aluminum specimen was imaged with a Skyscan 1072. Exposure time was 380 ms and the voxel size was 4.6 μm. The reconstruction center was accurately aligned in **c** and other figures were reconstructed with a misalignment specified in each figure. Misalignment value is + 10, +5, -5 and -10 in **a**, **b**, **d** and **e**, respectively

7.6.4 Artifacts Due to Reconstruction

Figure 7.43 shows artifacts formed when the reconstruction center was misaligned. Focusing on particles, pores, and protrusions on the surface generates artifacts in the shape of a tuning fork when the center of rotation is misaligned. The size of these artifacts increases with larger misalignment. The direction of this tuning fork inverts when misaligned in the reverse direction; therefore, this can be used to determine the direction towards which the center of rotation is misaligned. In either case, specifying the approximate coordinate of the center of rotation and conducting reconstruction, regardless of image quality, is the most fundamental element of X-ray tomography. Cross-sections, where structures such as particles or pores can serve as a reference point, should be sought when conducting an accurate reconstruction (Fig. 7.44).

References

1. Japanese Industrial Standards, Industrial X-ray CT devices—terminology. JIS **B7442** (2013)
2. Japanese Industrial Standards, Medical radiation devices—defined terminology. JIS **Z4005** (2012)
3. Medical Imaging Technology Handbook, Japanese Society of Medical Imaging Technology (2012). ISBN-13:978-4990666705
4. For example, Hamamatsu Photonics High-Performance Image Control System HiPic User Manual. http://www-bl20.spring8.or.jp/detectors/manual/. Accessed June 2018
5. SPring-8 BL20: How to make a transmission image movie (2010.07.06 version, txt format), http://www-bl20.spring8.or.jp/xct/manual/make-movie.txt. Accessed June 2018
6. ImageJ website, https://imagej.nih.gov/ij/docs/guide/146-26.html#toc-Subsection-26.6. Accessed June 2018
7. International Standard IEC, 62220-1, First edition, 2003–10, Medical electrical equipment—characteristics of digital X-ray imaging devices—Part 1: determination of the detective quantum efficiency
8. K.M. Hanson, in *Proceedings of SPIE 3336, Physics of Medical Imaging*, ed. by J.T. Dobbins III, J.M. Boone (1998), pp. 243–250
9. D.R. Dance, S. Christofides, A.D.A. Maidment, I.D. McLean, K.H. Ng, in *Diagnostic Radiology Physics A Handbook for Teachers and Students* (International atomic energy agency, 2014), p. 78
10. I. Elbakri, SU-GG-I-121: JDQE: A user—friendly ImageJ Plugin for DQE Calculation. Med. Phys. **37**, 3129 (2010)
11. CT Image Measurement Program CT measure Basic ver. 0.97b2 2016.8.22, Japanese Society of CT Technology, http://www.jsct-tech.org/index.php?page=member_ctmeasurefree. Accessed June 2018
12. Japanese Industrial Standards, Phantoms for X-Ray CT devices. JIS Z **4923** (2015)
13. K. Ichikawa, S. Muramatsu, Standard X-Ray CT image measurements (Ohmsha, 2018), p. 119
14. H. Toda, M. Kobayashi, T. Kubo, K. Moizumi, D. Sugiyama, Y. Yamamoto, T. Harada, K. Hayashi, Y. Hangai, Y. Murakami, J. Jpn. Instit. Light Metals **63**, 343–349 (2013)
15. F.R. Verdun, D. Racine, J.G. Ott, M.J. Tapiovaara, P. Toroi, F.O. Bochud, W.J.H. Veldkamp, A. Schegerer, R.W. Bouwman, I.H. Giron, N.W. Marshall, S. Edyvean, Physica Med. **31**, 823–843 (2015)
16. 10 spatial resolution in CT. J. ICRU, **12**, 1 (2012), Report 87. https://doi.org/10.1093/jicru/ndt001 (Oxford University Press)
17. Micro-CT Wire Phantom: QRM Gmbh, http://www.qrm.de/content/pdf/QRM-MicroCT-Wire.pdf. Accessed July 2018
18. T.M. Buzug, *Computed Tomography: From Photon Statistics to Modern Cone-Beam CT* (Springer, Berlin, Germany, 2008)
19. X-Ray CT Resolution Specimen Au Absorbent (JIMA RT CT-01) Catalog: Japan Inspection Instruments Manufacturers' Association (JIMA), http://www.jima.jp/content/pdf/catalog_rt_ct01_j.pdf. Accessed July 2018
20. MicroCT Bar Pattern Phantom: QRM Gmbh, http://www.qrm.de/content/pdf/QRM-MicroCT-Barpattern-Phantom.pdf. Accessed July 2018
21. D. Seo, F. Tomizato, H. Toda, K. Uesugi, A. Takeuchi, Y. Suzuki, M. Kobayashi, Appl. Phys. Lett. **101**, 261901 (2012)
22. K. Ichikawa, H. Kunitomo, T. Sakurai, K. Ohashi, M. Sugiyama, T. Miyaji, H. Fujita, Jpn. J. Radiologic. Technol. **58**, 1261–1267 (2002)
23. S.M. Bentzen, Med. Phys. **10**, 579–581 (1983)
24. F.F. Yin, M.L. Giger, K. Doi, Med. Phys. **17**, 960–966 (1990)
25. Photography—electronic still-picture cameras. Resolution measurements (2000(E)). ISO Standard 12233
26. P. Hammersberg, M. Mangard, J. X-ray Sci. Technol. **8**, 75–93 (1998)

27. P.M. Jenneson, R.D. Luggar, E.J. Morton, O. Gundogdu, U. Tuzun, J. Appl. Phys. **96**, 2889–2894 (2004)
28. Image J Plug-in Xlib, https://imagej.net/Xlib. Accessed Sept 2018
29. M. Kobayashi, Y. Sugihara, H. Toda, K. Uesugi, J. Jpn. Instit. Light Metals **63**, 273–278 (2013)